

A comparison of heat flow interpolation techniques

Buchanan C. Kerswell ¹Matthew J. Kohn ¹

¹Department of Geosciences, Boise State University, Boise, ID 83725

Key Points:

-
-
-

8 **Abstract**9 **1 Introduction**

10 Heat escaping the solid Earth's surface indicates a dynamically cooling planet. Surface
 11 heat flow databases (Hasterok & Chapman, 2008; Lucaleau, 2019; Pollack et al.,
 12 1993) provide a way to investigate and quantify geodynamics by relating the amount of
 13 heat escaping Earth's surface to heat-transferring and heat-generating subsurface pro-
 14 cesses such as diffusion, hydrothermal circulation, radioactive decay, fault motion, sub-
 15 duction dynamics, and mantle convection (Currie et al., 2004; Currie & Hyndman, 2006;
 16 Fourier, 1827; Furlong & Chapman, 2013; Furukawa, 1993; Gao & Wang, 2014; Hasterok,
 17 2013; Kerswell et al., 2020; Parsons & Sclater, 1977; Pollack & Chapman, 1977; Rud-
 18 nick et al., 1998; Stein & Stein, 1992, 1994; Wada & Wang, 2009). Surface heat flow ob-
 19 servations continue to motivate research, evident by more than 1,393 publications com-
 20 piled in the most recent heat flow dataset, although the rate of publications using sur-
 21 face heat flow has declined since the mid 1980's (Jennings & Hasterok, 2021).

22 Questions such as calculating the global surface heat flux from continents and oceans
 23 require interpolating discrete heat flow observations onto a continuous approximation
 24 of Earth's surface. Interpolation attempts commonly use one or more geographic, geo-
 25 logic, geochronologic, or geophysical proxies to predict heat flow at unknown locations
 26 by association with similar observation sites (e.g., bathymetry or elevation, proximity
 27 to active or ancient orogens, seafloor age, upper mantle shear wave velocities, Chapman
 28 & Pollack, 1975; Davies, 2013; Goutorbe et al., 2011; Lee & Uyeda, 1965; Lucaleau, 2019;
 29 Sclater & Francheteau, 1970; Shapiro & Ritzwoller, 2004). These methods are called *sim-*
 30 *ilarity methods* (Figure 1) and follow the assumptions embedded in the Third Law of Ge-
 31 ography: *the more similar the geographic configuration of two points, the more similar*
 32 *their values* (Zhu et al., 2018).

33 Using prior information in estimation is an advantage of the Third Law and is ar-
 34 guably the most reasonable approach for interpolating surface heat flow. Our understand-
 35 ing of geodynamics and near-surface heat flow perturbations implies a strong relation-
 36 ship between surface heat flow and the set of physical conditions (e.g., Goutorbe et al.,
 37 2011), irrespective of the location. For example, younger oceanic plates should have higher
 38 surface heat flow than older plates (Stein & Stein, 1992), subducting oceanic plates will

39 lower surface heat flow near trenches (Furukawa, 1993), and hydrothermal circulation
 40 of seawater can modify heat escaping from oceanic crust (Hasterok et al., 2011). Inter-
 41 polation by the Third Law makes reasoned predictions of heat flow with priors from many
 42 independently-tested geodynamic models. However, the Third Law is strongly biased to-
 43 wards such models and risk making determinations where, in fact, deviations from such
 44 models occur.

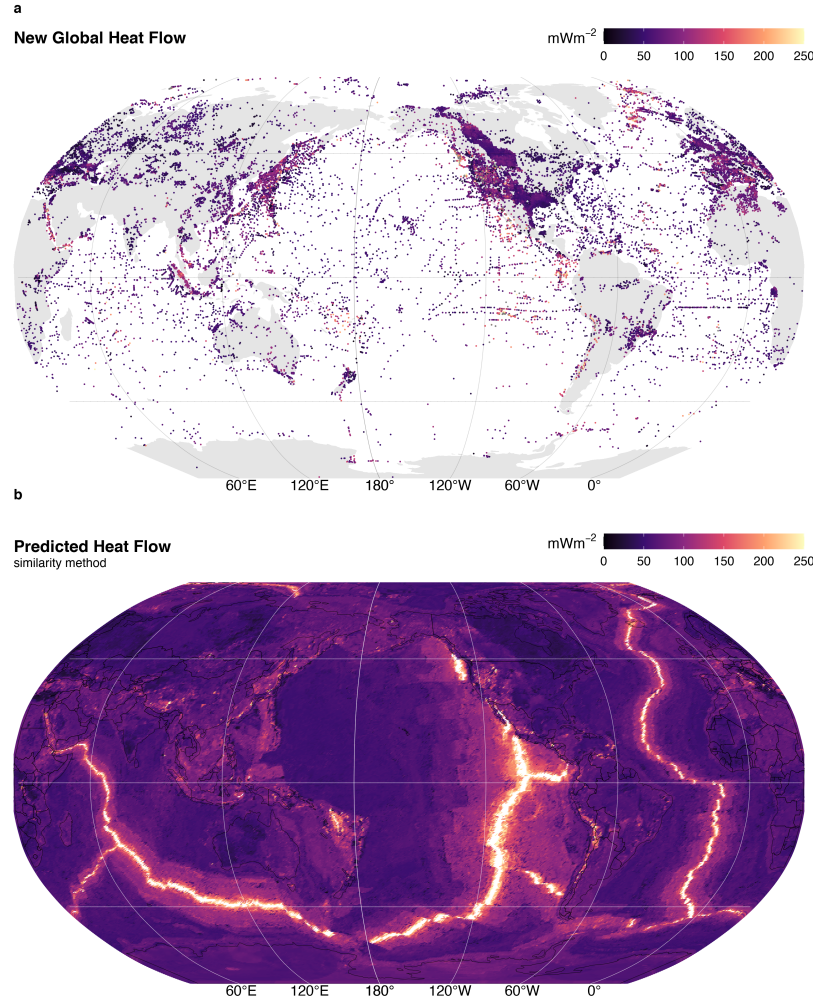


Figure 1: Global heat flow. (a) The NGHF dataset ($n = 69729$) and (b) interpolation by similarity method. Data from Luazeau (2019).

45 In contrast, there exists some degree of spatial dependence, or continuity, in the
 46 distribution of surface heat flow. A pair of surface heat flow observations taken one me-
 47 ter apart will be strongly correlated. The correlation between pairs of observations will
 48 likely decrease with increasing distance between the pairs (Goovaerts, 1997). This is en-

49 capsulated in the First Law of Geography: *everything is related, but nearer things are*
50 *more related* (Krige, 1951; Matheron, 1963). The spatial (dis)continuity of surface heat
51 flow represents the areal extent of geodynamic processes and their interactions. For ex-
52 ample, patterns of consistently low surface heat flow outline the areal extent of cratons
53 (Figure 1) and consistent patterns of heat flow near volcanic arcs are interpreted to re-
54 flect common backarc lithospheric thermal structures and slab-mantle mechanical cou-
55 pling depths in subduction zones (Furukawa, 1993; Kerswell et al., 2020; Wada & Wang,
56 2009).

57 Predicting surface heat flow by considering many nearby observations (i.e. Krig-
58 ing, Krige, 1951) is advantageous because the reality spatial dependence is conserved.
59 However, Kriging is disadvantageous because it assumes that the underlying distribu-
60 tion of heat flow is *stationary* (constant in space and time), which fails in geodynam-
61 ically complex regions. This problem is overcome by relaxing assumptions of stationar-
62 ity and applying techniques that respect the Second Law of Geography: *spatial phenom-*
63 *ena are inherently heterogenous* (Goodchild, 2004), such as directional Kriging or Markov-
64 Bayes techniques that include proxies as priors (Bárdossy, 1997).

65 In this study we attempt to answer the following questions: 1) What are the dif-
66 ferences between global heat flow interpolations predicted by Kriging and similarity meth-
67 ods? 2) What are the implications of the differences according to the implicit assump-
68 tions embodied in the First and Third Laws of Geography? 3) Which method is better
69 suited for hypothesis testing in studies sampling surface heat flow?

70 We first use ordinary Kriging to interpolate the New Global Heat Flow (NGHF)
71 dataset of Lucaleau (2019). Our method is optimized using a genetic algorithm that min-
72 imizes a cost function considering both the misfit on the variogram models and inter-
73 polation results (after Li et al., 2018). We then compare our interpolation results to those
74 of Lucaleau (2019) and consider the implications of Kriging vs. similarity methods of
75 interpolation. We restrict our comparison to areas near subduction zone segments de-
76 fined by Syracuse & Abers (2006) for two reasons: 1) to provide distributions and statis-
77 tics useful to subduction zone research, and 2) to emphasize differences and idiosyncrasies
78 in both interpolation approaches in a complex tectonic and thermal setting. We find that
79 the fidelity and usefulness of interpolations depend on the question being asked and the
80 choice of methodology.

81 **2 Methods**

82 **2.1 The NGHF Dataset**

83 The NGHF dataset was downloaded from the supplementary material of Lucaleau
 84 (2019). It contains 69729 data points, their locations in latitude/longitude, and metadata—
 85 including a data quality rank (Code 6) from A to D (with Code 6 = Z = undetermined).
 86 The reader is referred to Lucaleau (2019) for details on compilation, references, and his-
 87 torical perspective on the NGHF and previous compilations. We use NGFH because it
 88 is the most recent dataset available, has been carefully compiled, and is open-access.

89 Like Lucaleau (2019), we exclude 4790 poor quality observations (Code 6 = D) from
 90 our analysis. We further remove 350 data points without heat flow observations and two
 91 without geographic information. Multiple observations at the same location are parsed
 92 to avoid singular covariance matrices during Kriging:

$$\begin{aligned}
 f(X_i^q, Y_i^q) = & \\
 X_i^q > Y_i^q \rightarrow z_i = x_i & \\
 X_i^q < Y_i^q \rightarrow z_i = y_i & \\
 X_i^q = Y_i^q \rightarrow z_i = RAND(x_i, y_i) &
 \end{aligned} \tag{1}$$

93 where X_i^q and Y_i^q represent the quality of each duplicate observation pair at loca-
 94 tion i , $RAND$ is a random function that selects either the observation x_i or y_i , and z_i
 95 stores the observation selected by $f(X_i^q, Y_i^q)$. The final dataset used for Kriging has $n =$
 96 55274 observations after parsing $n = 32430$ duplicate observation.

97 **2.2 Kriging**

98 Kriging is a three-step process that involves first estimating an experimental vari-
 99 iogram, $\hat{\gamma}(h)$, fitting the experimental variogram with one of many variogram models,
 100 $\gamma(h)$, and finally using the modelled variogram to predict random variables at unknown
 101 locations (Cressie, 2015; Krige, 1951). We use the general-purpose functions defined in
 102 the “R” package `gstat` (Gräler et al., 2016; Pebesma, 2004) to perform all three steps.
 103 We begin by estimating an experimental variogram as defined by Bárdossy (1997):

$$\hat{\gamma}(h) = \frac{1}{2N(h)} \sum_{N(h)} (Z(u_i) - Z(u_j))^2 \quad (2)$$

where $N(h)$ is the number of pairs of points, $Z(u_i)$ and $Z(u_j)$, separated by a lag distance, $h = |u_i - u_j|$. We evaluate $\hat{\gamma}(h)$ at fifteen lag distances by binning the irregular spaced data with a bin width, δ , equal to a proportion of the maximum lag distance, c , divided by the number of lags used to evaluate the variogram. The lag cutoff parameter, c , is optimized by genetic algorithm (discussed below). The binwidth is then $\delta = \max(N(h))/(15c)$, and $N(h) \leftarrow N(h, \delta h) = \{i, j : |u_i - u_j| \in [h - \delta h, h + \delta h]\}$. In simple terms, Equation 2 represents the similarity, or dissimilarity, between pairs of observations in space. Equation 2 is adheres to the First Law of Geography and is derived from the theory of *regionalized variables* (Matheron, 1963, 2019), which formally defines a probabilistic framework for spatial interpolation of natural phenomena. It is important for the reader to understand the fundamental assumptions implicit in Equation 2 in order to understand the comparison of interpolation techniques discussed later. The basic assumptions used in our Kriging method are:

- $\hat{\gamma}(h)$ is directionally invariant (isotropic)
- $\hat{\gamma}(h)$ is evaluated in two-dimensions and neglects elevation, $Z(u) \in \mathbb{R}^2$
- The first and second moments of $Z(u)$ have the following conditions over the domain D :

$$\begin{aligned} E[Z(u)] &= \text{mean} = \text{constant}, & \forall u \in D \\ E[(Z(u + h) - \text{mean})(Z(u) - \text{mean})] &= C(h), & \forall |u, u + h| \in D \end{aligned} \quad (3)$$

The last assumption (Equation 3) is called “second-order stationarity” and is implicit in the First Law of Geography. It assumes the underlying probability distribution of the random variable, $Z(u)$, does not change in space and the covariance, $C(h)$, only depends on the distance, h , between two random variables. These assumptions are expected to be valid in cases where the underlying natural process is stochastic, spatially continuous, and has the property of additivity such that $\frac{1}{n} \sum_{i=1}^n Z(u_i)$ has the same meaning as $Z(u)$ (Bárdossy, 1997).

The following are two illustrative cases where Equation 3 is likely valid:

- 129 1. The thickness of a sedimentary unit with a homogeneous concentration of radioac-
 130 tive elements can be approximated by $q_s = q_b + \int A dz$, where q_b is a constant
 131 heat flux entering the bottom of the layer and A is the heat production within the
 132 layer with thickness z (Furlong & Chapman, 2013). If we have two samples, $Z(u_1) =$
 133 31 mW/m^2 and $Z(u_2) = 30.5 \text{ mW/m}^2$, their corresponding thicknesses would
 134 be $Z'(u_1) = 1000 \text{ m}$ and $Z'(u_2) = 500 \text{ m}$ for $A = 0.001 \text{ mW/m}^3$ and $q_b =$
 135 30 mW/m^2 . The variable, $Z(u)$, in this case is additive because the arithmetic mean
 136 of the samples is a good approximation of the average sedimentary layer thickness,
 137 $(Z(u_1) + Z(u_2))/2 = 750 \text{ m}$.
- 138 2. The age of young oceanic lithosphere can be approximated by $q_s(t) = kT_b(\pi\kappa t)^{-1/2}$,
 139 where $q_s(t)$ is the surface heat flow of a plate with age, t , T_b is the temperature
 140 at the base of the plate, k is thermal conductivity, and $\kappa = k/\rho C_p$ is thermal dif-
 141 fusivity (Stein & Stein, 1992). For $k = 3.138 \text{ W/mK}$, $\rho = 3330 \text{ kg/m}^3$, $C_p =$
 142 1171 J/kgK , $T_b = 1350^\circ\text{C}$, two samples, $Z(u_1) = 180 \text{ mW/m}^2$ and $Z(u_2) =$
 143 190 mW/m^2 , would correspond to plates with ages of $Z'(u_1) = 10 \text{ Ma}$, and $Z'(u_2) =$
 144 9 Ma , respectively. Since $Z(u_1)+Z(u_2)/2 = 185 \text{ mW/m}^2$ and $Z'(185 \text{ mW/m}^2) =$
 145 $9.5 \text{ Ma} = Z'(u_1) + Z'(u_2)/2$, the variable $Z(u)$ in this case is also additive.

146 In contrast, Equation 3 is likely invalid in regions that transition among two or more
 147 tectonic regimes. For example, the expected heat flow $E[Z(u)] = \text{mean}$ will change when
 148 moving from a spreading center to a subduction zone. $E[Z(u)] = \text{mean} \neq \text{constant}$
 149 over the region of interest. Proceeding with Equation 3 in this case has the effect of mask-
 150 ing the geodynamic complexity. In other words, the First Law of Geography is violated
 151 and the geodynamic complexity will be *invisible* to Kriging predictions unless heatflow
 152 observations are sufficiently dense. We will see that this has important implications when
 153 comparing our Kriging method to Lucazeau (2019)'s interpolation method, which is ex-
 154 actly opposite of this formalism—it only considers the similarities among physical prox-
 155 ties and not spatial dependence.

156 The second step is to fit the experimental variogram with a variogram model, $\gamma(h)$.
 157 In this study we fit two popular variogram models to the experimental variogram. We
 158 use models with sill, which implies the spatial dependence between pairs of points has
 159 a finite range. The spherical and exponential variogram models used in this study are
 160 defined as (Chiles & Delfiner, 2009; Cressie, 2015):

$$sph \leftarrow \gamma(h) = \begin{cases} n + s \left(\frac{3h}{2a} - \frac{1}{2} \left(\frac{h}{a} \right)^3 \right), & \text{if } 0 \leq h \leq a \\ n + s, & \text{if } h > a \end{cases} \quad (4)$$

$$exp \leftarrow \gamma(h) = n + s \left(1 - exp \left(\frac{-h}{a} \right) \right), \quad \text{if } h \geq 0$$

161 where n is the nugget, s is the sill, and a is the effective range. The effective range,
 162 a , is related to the range, r , by $a = r$ and $a = r/3$ for spherical and exponential mod-
 163 els, respectively (Gräler et al., 2016; Pebesma, 2004). We use the function `fit.variogram`
 164 in `gstat` to try both variogram models. The best model is selected by the minimum mis-
 165 fit by weighted least square (WLS, Pebesma, 2004).

166 We use ordinary Kriging for our interpolation step, which predicts the value of a
 167 random function, $\hat{Z}(u)$, at unknown locations as a linear combination of all known lo-
 168 cations in the domain, D (Bárdossy, 1997):

$$\hat{Z}(u) = \sum_{i=1}^n \lambda_i Z(u_i), \quad \forall u \in D \quad (5)$$

169 The conditions in Equation 3 set up a constrained minimization problem since one
 170 has:

$$E[Z(u)] = mean, \quad \forall u \in D \quad (6)$$

171 The linear estimator must obey

$$E[\hat{Z}(u)] = \sum_{i=1}^n \lambda_i E[Z(u_i)] = mean \quad (7)$$

172 so the weights must be

$$\sum_{i=1}^n \lambda_i = 1 \quad (8)$$

173 This is the first constraint, also known as the unbiased condition, which states that
 174 the sum of the weights must equal one. However, there is an infinite set of real numbers
 175 one could use for the weights, λ_i . Our goal is to find the set of weights in Equation 5 that

176 minimizes the estimation variance. This can be solved by minimizing the covariance func-
 177 tion, $C(h)$ from Equation 3:

$$\begin{aligned}\sigma^2(u) &= \text{Var}[Z(u) - \hat{Z}(u)] = E \left[(Z(u) - \sum_{i=1}^n \lambda_i Z(u_i))^2 \right] = \\ &E \left[Z(u)^2 + \sum_{j=1}^n \sum_{i=1}^n \lambda_j \lambda_i Z(u_j) Z(u_i) - 2 \sum_{i=1}^n \lambda_i Z(u_i) Z(u) \right] = \\ &C(0) + \sum_{j=1}^n \sum_{i=1}^n \lambda_j \lambda_i C(u_i - u_j) - 2 \sum_{i=1}^n \lambda_i C(u_i - u)\end{aligned}\quad (9)$$

178 Minimizing Equation 9 with respect to the unbiased condition (Equation 8), yields
 179 the best linear unbiased estimator (BLUE, Bárdossy, 1997) for Equation 5 and together
 180 are considered the Kriging system. In our case, this is done by the function `krige` in `gstat`.

181 2.3 Kriging Optimization

182 Achieving a useful Kriging results depends on one's choice of many Kriging param-
 183 eters (Θ). In this study, we investigate a set of parameters, Θ :

$$\Theta = \{c, w, m, s, a, n, S\} \quad (10)$$

184 where c is the lag cutoff proportion, w is the lag window, m is the model type (sph
 185 or exp), s is the sill, a is the effective range, n is the nugget, and S is the maximum dis-
 186 tance for local Kriging. Only points within S from the prediction location are used for
 187 Kriging. The lag cutoff is the maximum separation distance between pairs of points used
 188 in the experimental variogram (i.e. the x-axis maximum limit) calculated as a fraction
 189 of the overall maximum separation distance for all observations, $Z(u)$, in the domain,
 190 D . The lag window, w , shifts the lags where the variogram is evaluated by removing the
 191 first n lags and adding n lags to the right side of the variogram. This is necessary to avoid
 192 negative ranges, a , when fitting experimental variograms with anomalously high vari-
 193 ances at small lag distances.

194 Our goal is to find Θ such that our interpolation, $f(x_i; \Theta)$, gives the most useful
 195 outcome—defined by minimizing a cost function, $C(\Theta)$, that represents the error between
 196 the set of real observations, $Z(u_i)$ and predictions, $\hat{Z}(u)$. We define a cost function that

197 simultaneously considers the misfit between the experimental and modelled variogram
 198 and between the Kriging predictions and observed heat flow (after Li et al., 2018):

$$C(\Theta) = (1 - w)C_F(\Theta) + wC_I(\Theta) \quad (11)$$

199 where $C_F(\Theta)$ is the root mean square error (RMSE) of the modelled variogram fit
 200 calculated by WLS, and $C_I(\Theta)$ is the RMSE of the Kriging result calculated by cross-
 201 validation. The weight, w , is set to 0.5 in our study, which balances the effects of $C_F(\Theta)$
 202 and $C_I(\Theta)$ on the cost function. The final expression to minimize becomes:

$$C(\Theta) = \frac{1-w}{\sigma_E} \sqrt{\frac{1}{N(h)} \sum_{k=1}^N w(h_k)[\hat{\gamma}(h_k) - \gamma(h_k; \Theta)]^2} + \frac{w}{\sigma_S} \sqrt{\frac{1}{M} \sum_{i=1}^M [Z(u_i) - \hat{Z}(u_i; \Theta)]^2} \quad (12)$$

203 where $N(h)$ is the number of pairs of points used to calculate the experimental var-
 204 iogram, $\hat{\gamma}(h_k)$, σ_E is the standard deviation of the experimental variogram, $\hat{\gamma}(h)$, $w(h_k)$
 205 is the weight in WLS and defines the importance of the k th lag in the error estimate.
 206 We use $w(h_k) = N_k/h_k^2$. $Z(u_i)$ and $\hat{Z}(u_i; \Theta)$ are the measured and predicted values,
 207 respectively, σ_s is the standard deviation of the predicted values, $\hat{Z}(u_i)$, and M is the
 208 number of measurements in $Z(u_i)$. For $C_I(\Theta)$ we use ten-fold cross-validation, which splits
 209 the dataset, $|Z(u_i), \forall u_i \in D|$ into ten equal intervals and tests one interval against the
 210 remaining nine. This process is then repeated over all intervals so that the whole dataset
 211 has been cross-validated.

212 Minimization of $C(\Theta)$ is achieved by a genetic algorithm that simulates biologic
 213 natural selection by differential success (Goldberg, 1989). Our procedure is as follows:

- 214 1. Initiate fifty *chromosomes*, ξ , with random starting parameters defined within the
 215 search domain (Table 1)
- 216 2. Evaluate the fitness of each individual chromosome as $-C(\Theta)$ for the entire pop-
 217 ulation
- 218 3. Allow the population to exchange genetic information by sequentially performing
 219 genetic operations:
- 220 a. Selection: the top 5% fittest chromosomes survive each generation

- 221 b. Crossover: pairs of chromosomes have an 80% chance of exchanging genetic in-
 222 formation
- 223 c. Mutation: there is a 10% chance for random genetic mutations
- 224 4. Evaluate the fitness of the new population
- 225 5. If the termination criterion is met, do step (6), otherwise continue to evolve by
 226 repeating steps (3) and (4)
- 227 6. Decode the best chromosome and build the optimal variogram

228 We use the general-purpose functions in the “R” package **GA** (Scrucca, 2013, 2016)
 229 to perform each step in the above procedure.

Table 1: Parameters and ranges used in the optimization algorithm

Parameter	Search Domain	Units
Lag Cutoff (c)	[1/3, 1/15]	NA
Lag Window (w)	[1, 5]	NA
Model (m)	[Spherical, Exponential]	NA
Sill (s)	[1, 1000 $\sqrt{2}$]	mWm^{-2}
Effective Range (a)	[1, 1000]	km
Nugget (n)	[1, 1000 $\sqrt{2}$]	mWm^{-2}
Local Search (S)	[1, 1000]	km

230 2.4 Map Projection and Interpolation Grid

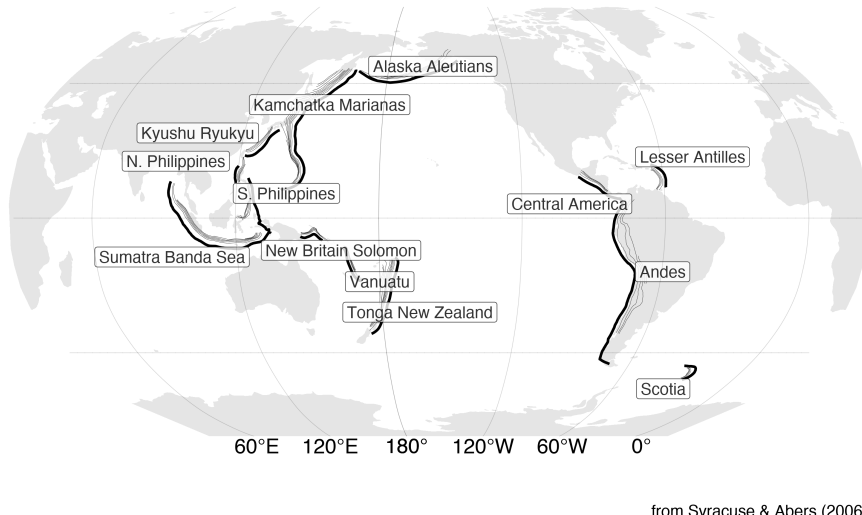
231 We interpolate onto the same 0.5°C x 0.5°C grid as Luazeau (2019) so a direct
 232 difference could be calculated between our interpolation methods and Luazeau (2019)’s.
 233 The NGHF and grid with predicted heat flow from Luazeau (2019) were transformed
 234 into a Pacific-centered Robinson coordinate reference system (CRS) defined using the
 235 `proj` string (PROJ contributors, 2021):

236 `+proj=robin +lon_0=-155 +lon_wrap=-155 +x_0=0 +y_0=0`
 237 `+ellps=WGS84 +datum=WGS84 +units=m +no_defs`

238 All geographic operations, including Kriging and taking the difference with Lucaleau
239 (2019)'s heat flow predictions, are performed in the above CRS using the general-purpose
240 functions in the "R" package **sf** (Pebesma, 2018). We define the Kriging domain near
241 individual arc segments in two steps: 1) 1000 km buffers are drawn around the arc seg-
242 ments as defined by Syracuse & Abers (2006). 2) The bounding box of the 1000 km buffer
243 is expanded by 10% on all sides (Figure 2). We use Lucaleau (2019)'s grid for Kriging
244 predictions so differences can be taken point-by-point at the exact same locations.

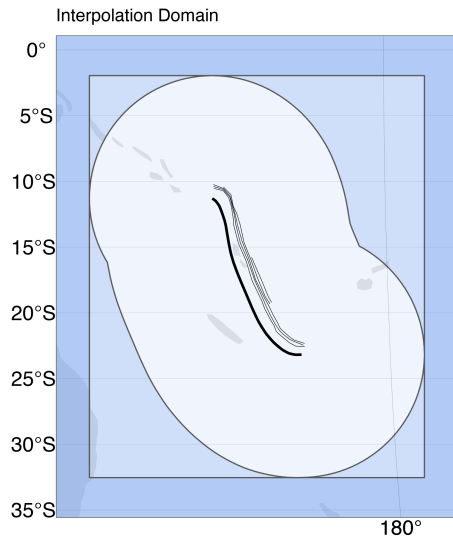
245 We provide the complete NGHF dataset (Lucaleau, 2019), filtered and parsed NGHF
246 dataset, heat flow interpolations (from Lucaleau, 2019, and this study), and our code
247 as supplementary information to support FAIR data policy (Wilkinson et al., 2016). These
248 materials can also be retrieved from the official repository at [https://doi.org/10.17605/](https://doi.org/10.17605/OSF.IO/CA6ZU)
249 [OSF.IO/CA6ZU](https://osf.io/ca6zu/).

a Subduction Zone Segments



from Syracuse & Abers (2006)

b Vanuatu



c Vanuatu

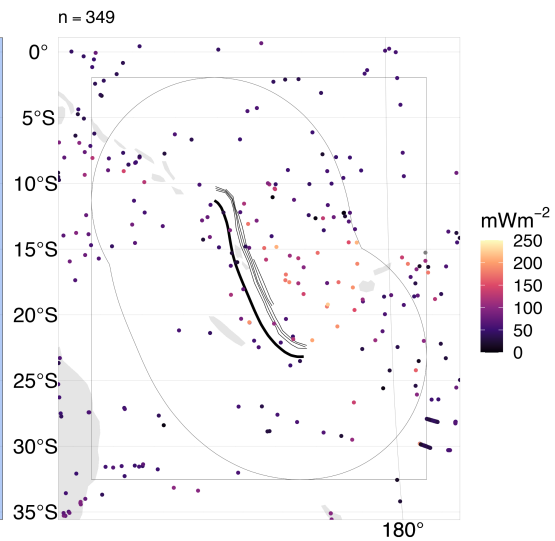


Figure 2: Subduction zone segments and interpolation domain. (a) Heat flow is interpolated around thirteen subduction zone segments by (b) drawing a 1000km buffer (lightest blue) around each segment and expanding the buffer's bounding box (medium blue) by 10% on all sides (darkest blue). (c) The NGHF dataset is cropped within the largest rectangle. Data from Syracuse & Abers (2006) and Lucazeau (2019).

250 **3 Results**251 **3.1 Heat Flow Near Subduction Zone Segments**

252 Summary statistics for surface heat flow observations by subduction zone segment
 253 are given in Table 2 and Figure 3. Surface heat flow is median-centered around 45-70
 254 mWm^{-2} and narrowly distributed (excluding outliers) with inter-quartile ranges (IQR)
 255 from 12 to 50 mWm^{-2} for most subduction zone segments. Alaska Aleutians is the ex-
 256 ception with a higher median of 184 mWm^{-2} and broader range (IQR = 250 mW^{-2}).
 257 The whole distributions (including outliers) for all segments are strongly right-skewed
 258 with maximum heat flow values of several thousand of mWm^{-2} or more. Heat flow val-
 259 ues above 250 mWm^{-2} are considered geothermal areas by Lucaleau (2019), which we
 260 adopt as a relevant empirical limit for anomalously high heat flow.

Table 2: Heat flow (mWm^{-2}) observations

Segment	n	Min	Max	Median	IQR	Mean	Sigma
Alaska Aleutians	2791	4	7765	184	206	233	345
Andes	5226	7	911	45	50	87	89
Central America	5033	8	911	45	48	88	91
Kamchatka Marianas	3958	1	25200	71	48	118	582
Kyushu Ryukyu	3247	1	25200	72	44	126	642
Lesser Antilles	3535	13	1150	41	13	52	50
N. Philippines	1002	3	25200	72	35	195	1127
New Britain Solomon	180	3	174	64	42	69	30
S. Philippines	1444	1	25200	71	43	158	938
Scotia	72	13	145	76	23	74	28
Sumatra Banda Sea	3039	1	1350	65	47	76	67
Tonga New Zealand	507	2	416	54	40	64	45
Vanuatu	349	2	283	54	40	64	44

261 **3.2 Variogram Models**

262 The optimal variogram models and associated errors $C_F(\Theta)$ and $C_I(\Theta)$ are given
 263 in Table 3. Almost twice as many experimental variograms are fit with spherical mod-

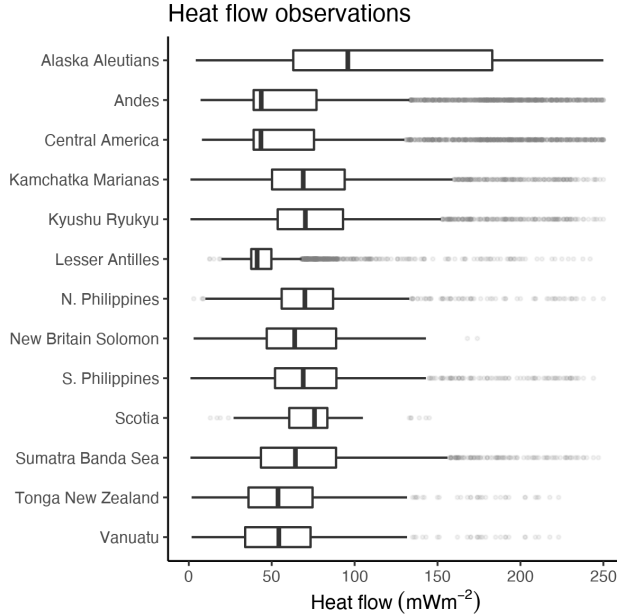


Figure 3: Distribution of heat flow observations. Heat flow near most segments is centered around $50 \text{ } mW m^{-2}$ and highly skewed right (shadowy dot outliers). The skewness likely represents sampling near geothermal systems, volcanic arcs, or spreading centers. Data from Lucaleau (2019).

els (8) compared to exponential models (5). Variogram model sills vary substantially among the subduction zone segments between 9 and $1538 \text{ } mW m^{-2}$. Variogram model ranges also vary substantially among segments from 4 to 1676 km .

No apparent correlation exists between variogram model range and subduction zone segment length, number of heat flow observations, nor domain area (Figure 4). Most subduction zone segments show spatial dependence of a few hundred kilometers or less, irrespective of the number of observations or segment size. The exceptions are Kyushu Ryukyu (range = 1774 km) and Vanuatu (range = 573 km), whose model variogram ranges are, perhaps, anomalously high.

Table 3: Optimal varigram models

Segment	Model	Sill [$mW m^{-2}$]	Range [km]
Alaska Aleutians	Sph	285	221
Andes	Sph	87	346
Central America	Sph	86	343
Kamchatka Marianas	Exp	612	271

Segment	Model	Sill [mWm^{-2}]	Range [km]
Kyushu Ryukyu	Sph	813	1774
Lesser Antilles	Exp	38	104
N Philippines	Sph	1198	238
New Britain Solomon	Exp	29	89
S Philippines	Sph	1026	414
Scotia	Exp	9	4
Sumatra Banda Sea	Sph	67	133
Tonga New Zealand	Sph	47	131
Vanuatu	Sph	48	573

3.3 Interpolation Comparison

Summary statistics for the interpolation differences are given in Table 4 and Figure 5. Note that the difference is taken at the exact same locations for every prediction. Differences between the similarity method and Kriging are small for most segments with the exception of Central America, which shows a broader distribution of differences than the other segments. The median differences range from -9 to 7 mWm^{-2} with inter quartile ranges from 15 to 62 mWm^{-2} . Similar to the distribution of heat flow in these areas, the minimum and maximum difference in predicted heat flow are extreme and represent the failure of one method to predict extreme outliers of the other.

Table 4: Predicted heat flow (mWm^{-2}) differences

Segment	Min	Max	Median	IQR	Mean	Sigma
Alaska Aleutians	-550	2659	-2	20	3	71
Andes	-241	2336	2	35	12	72
Central America	-242	2731	8	63	43	147
Kamchatka Marianas	-2434	297	4	15	4	39
Kyushu Ryukyu	-2435	136	6	24	2	74
Lesser Antilles	-148	566	0	16	5	31
N Philippines	-2131	283	2	24	-1	67
New Britain Solomon	-81	236	2	22	5	20

Segment	Min	Max	Median	IQR	Mean	Sigma
S Philippines	-273	369	5	26	7	30
Scotia	-62	1001	-4	24	5	33
Sumatra Banda Sea	-312	386	0	20	2	20
Tonga New Zealand	-113	1695	-9	23	-2	30
Vanuatu	-166	1657	7	27	8	40

282 Prediction differences are either approximately normally distributed, or skewed right.
 283 Right skew and a tendency of medians to deviate positively from zero both reflect a sys-
 284 tematic overprediction of heat flow by the similarity method compared to Kriging (Fig-
 285 ure 5). However, Alaska Aleutians, Scotia, and Tonga New Zealand have negative me-
 286 dian differences. While there is a tendency for the similarity method to overpredict heat
 287 flow compared to Kriging, it is not true in every case.

288 Notable sources of prediction differences include 1) tectonic features predicted by
 289 similarity that are absent from Kriging or 2) general discordance between the spatial con-
 290 tinuity of heat flow observations and similarity predictions. For example, high heat flow
 291 representing Galápagos triple junction is predicted by similarity to the SW of the Cen-
 292 tral America segment (Figure 6 a). However, none of the triple junction arms, nor the
 293 Galápagos hot spot, are well defined in the Kriged prediction (Figure 6 b). The inter-
 294 polation comparison for Central America highlights two distinct regions—bright differ-
 295 ences along the arms of the triple junction and muted agreement to the E and NE of the
 296 Cocos Plate (Figure 6 c). Note the moderate differences within the Cocos Plate in Fig-
 297 ure 6 a where similarity predicts high heat flow by proximity to the nearby spreading
 298 centers, but heat flow in the region is, in fact, relatively low (compare Figure 6 a, b, c).
 299 Similar discordance between high similarity predictions and low heat flow observations
 300 are observed in many subduction zone segments, especially near spreading centers pre-
 301 dicted by similarity (e.g. Figure 12; see sec. 5).

302 On the other side of the Caribbean Plate, near the Lesser Antilles segment, sim-
 303 ilarity and Kriging predictions show good agreement. The Mid-Atlantic Ridge to the E
 304 appears in both predictions (Figure 7 a, b). The spreading center is better defined with
 305 Kriging in this case, as compared to the Galápagos triple junction, because the obser-
 306 vational density and spatial coverage near the Lesser Antilles segment are sufficiently high

Variogram range correlations

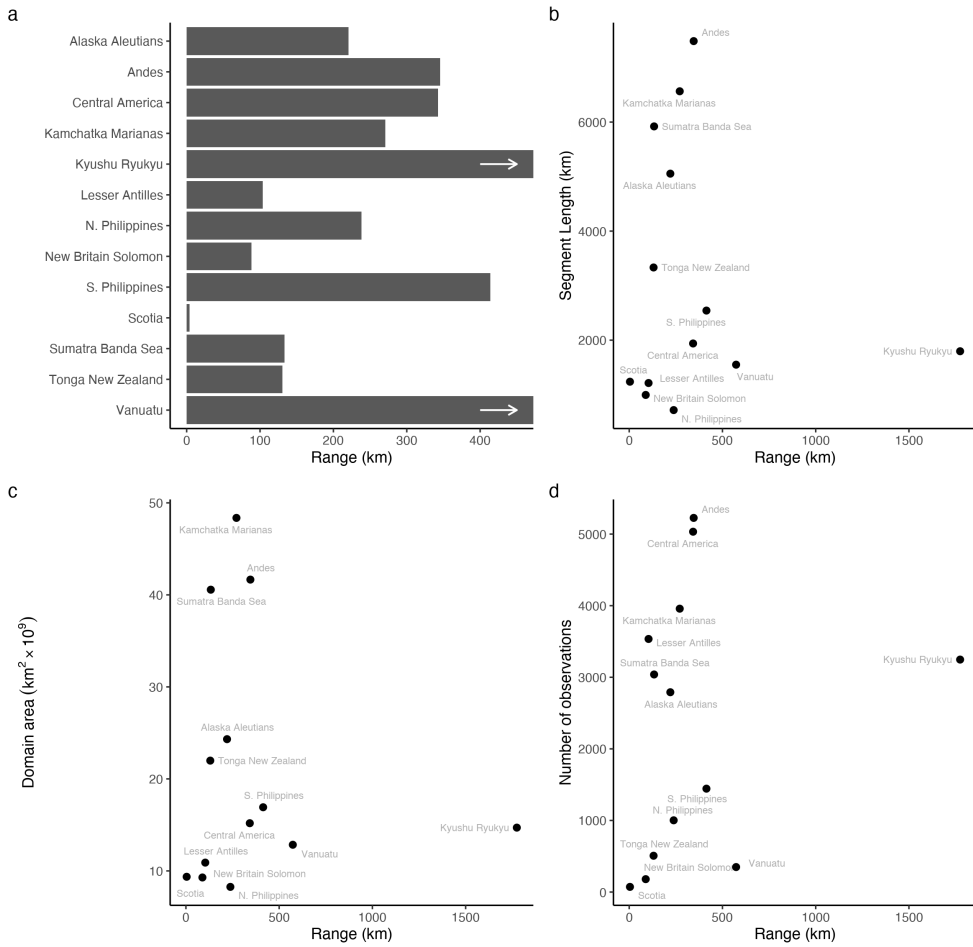


Figure 4: Summary of variogram model ranges and correlations with other features. (a) Variogram model ranges are variable, but generally below 400 km. Variogram model ranges show no correlation with segment length (b), number of heat flow observations (c), nor domain area (d). The spatial dependence of heat flow is apparently independent of these parameters.

and continuous near the Mid-Atlantic Ridge (see sec. 5). However, the comparison still highlight spreading centers as similarity tends to predict higher heat flow than observations.

Another example of good agreement between similarity and Kriging are interpolations near the Sumatra Banda Sea segment (Figure 8; Figure 20). Note the textural and structural complexity predicted by similarity (Figure 8 a) compared to the smooth featureless Kriging predictions (Figure 8 b). Despite the textural and structural differences, the difference between similarity and Kriging within the Sunda Plate, Australian Plate, and W Philippine Sea Plate is small (Figure 8 c).

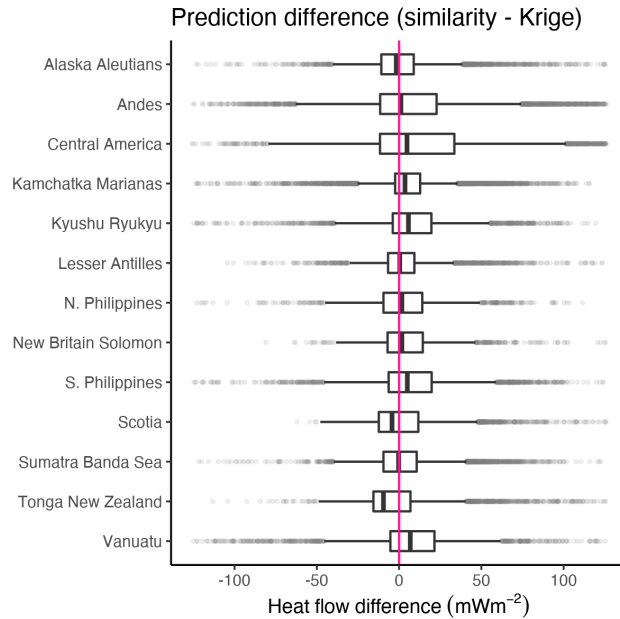


Figure 5: Point-by-point differences of predicted heat flow between similarity and Kriging interpolations. The differences for most subduction zone segments are median-centered at or near-zero with IQRs from 16 to 62. Outliers (shadowy dots) extend to extreme positive and negative differences.

316 Heat flow predictions near the Scotia segment illustrate a case where heat flow ob-
 317 servations are incredibly sparse. Similarity predicts high heat flow from the East Sco-
 318 tia Ridge (ESR) and the WSW-ENE trending transform boundary separating the Sco-
 319 tia and Sandwich Plates from the Antarctic Plate (Figure 9 a). Figure 9 b appears fea-
 320 tureless because very few heat flow observations ($n = 72$) define a flat experimental var-
 321 iogram for all lag distances greater than four kilometers (no spatial dependence beyond
 322 4 km, Table 3; Figure 21). Kriging predicts the expected (mean) heat flow value for the
 323 entire domain (Figure 9 b), in this case, according to Equation 5. Interestingly, the ex-
 324 pected heat flow is a fine predictor for most of the ocean basin, except near the spread-
 325 ing center and transform fault (Figure 9 c). The New Britain Solomon segment shows
 326 a similar comparison (Figure 18) with good agreement between similarity and Kriging
 327 despite very few heat flow observations, little spatial dependence (small variogram range),
 328 and a featureless Kriged interpolation.

329 While similarity tends to define tectonic features and Kriging tends to smooth out
 330 tectonic features, we find the opposite pattern within the tectonically-complex region near
 331 Vanuatu. Similarity predicts the N-S trending spreading center separating the New He-
 332 brides plate from the Balmoral Reef and Conway Reef microplates (Figure 10 a). How-

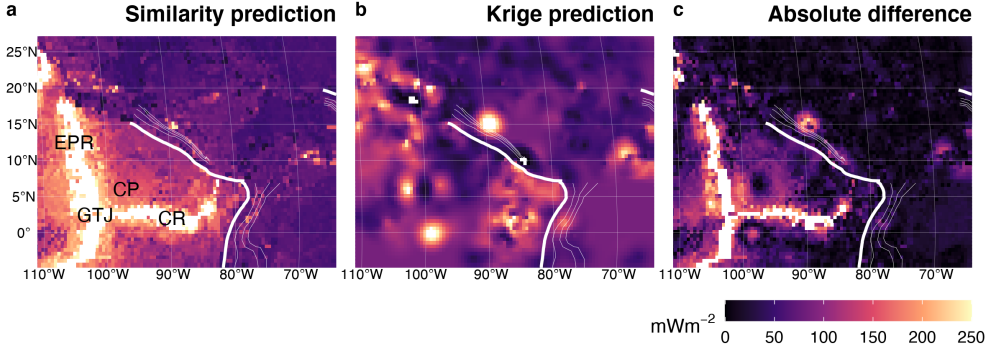


Figure 6: Similarity vs. Kriging predictions for Central America. The Galápagos triple junction (GTJ), East Pacific Rise (EPR), and Cocos Ridge (CR) are predicted by similarity (a), but not by Kriging (b). Note the moderate difference between predictions within the Cocos Plate (CP) where similarity predicts high heat flow but observations are low (c). Bold and thin white lines represent the subduction zone segment boundary and plate depth, respectively, as defined by Syracuse & Abers (2006). Heat flow data and similarity prediction from Lucaleau (2019).

333 ever, heat flow observations are sufficiently dense and continuous to partially resolve the
 334 short ridge segments and transform faults outlining the microplates between Vanuatu
 335 and the Tonga New Zealand segments by Kriging (Figure 10 b). The differences (Fig-
 336 ure 10 c) are difficult to interpret because of the somewhat random discordance between
 337 interpolation methods.

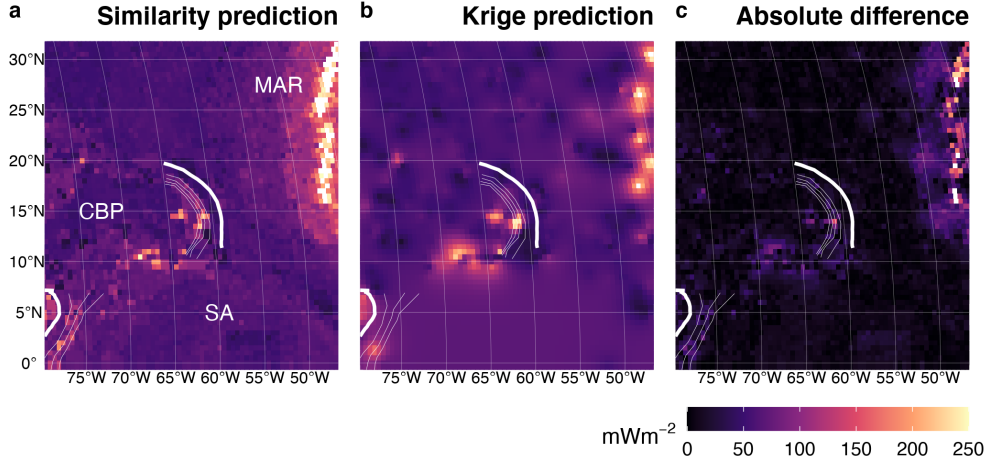


Figure 7: Similarity vs. Kriging predictions for the Lesser Antilles. The Mid-Atlantic Ridge (MAR) predicted by similarity (a) is also defined by Kriging (b) because of adequate observational density and spatial coverage near the spreading center. Good agreement between similarity and Kriging exist for the entire domain (c). CBP = Caribbean Plate, SA = South America. Bold and thin white lines represent the subduction zone segment boundary and plate depth, respectively, as defined by Syracuse & Abers (2006). Heat flow data and similarity prediction from Lucaleau (2019).

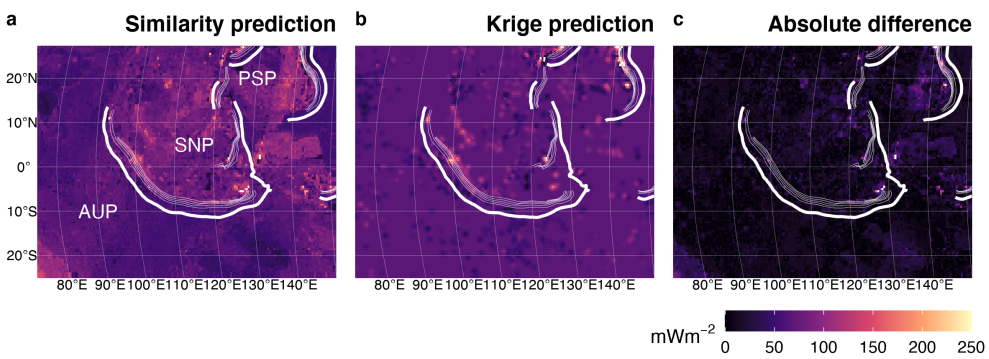


Figure 8: Similarity vs. Kriging predictions for Sumatra Banda Sea. Similarity predictions are texurally and structurally complex (a), while Kriging is smooth and featureless (b). Despite the textual and structural difference, the interpolations are similar, especially within the Sunda Plate (SNP), Australian Plate (AUP) and W Philippine Sea Plate (PSP). Bold and thin white lines represent the subduction zone segment boundary and plate depth, respectively, as defined by Syracuse & Abers (2006). Heat flow data and similarity prediction from Lucaleau (2019).

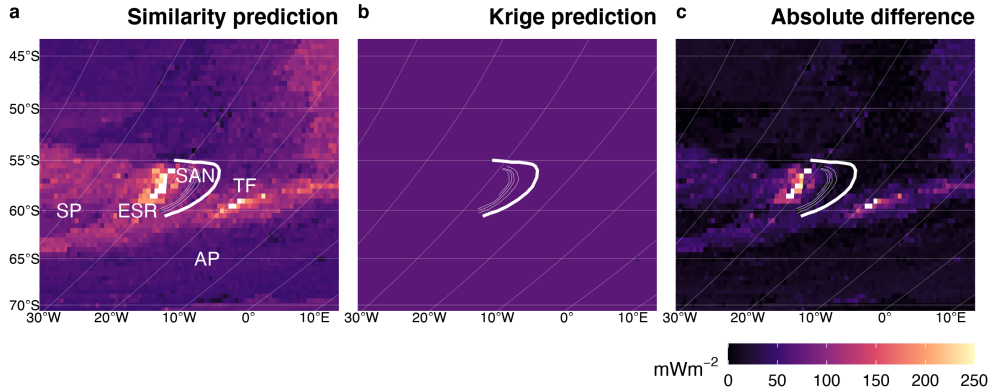


Figure 9: Similarity vs. Kriging predictions for Scotia. (a) Similarity predicts high heat flow for two tectonic features, the East Scotia Ridge (ESR) and a transform fault (TF) separating the Scotia and Sandwich Plates (SP, SAN) from the Antarctic Plate (AP). Kriging (b) is featureless because of incredibly sparse data. Despite few heat flow observations. Kriging predictions are only significantly different than similarity predictions near the ESR and transform fault (c). Bold and thin white lines represent the subduction zone segment boundary and plate depth, respectively, as defined by Syracuse & Abers (2006). Heat flow data and similarity prediction from Lucaleau (2019).

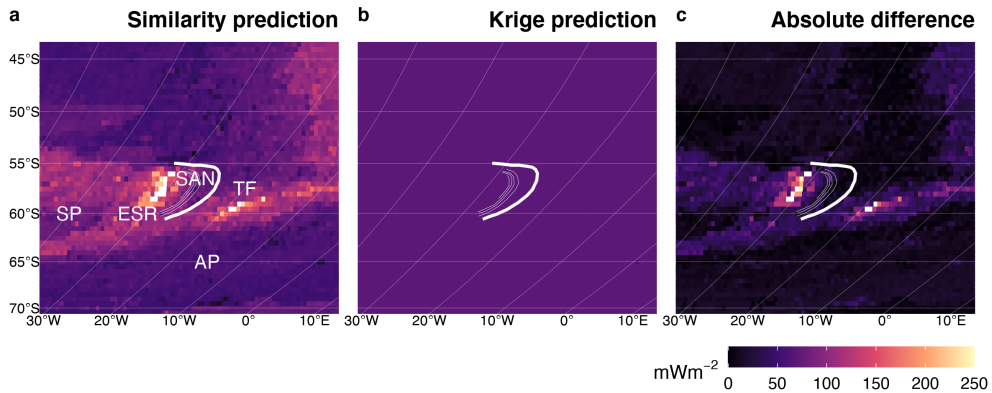


Figure 10: Similarity vs. Kriging predictions for Vanuatu. (a) Similarity resolved the spreading center separating the New Hebrides Plate (NHP) from the Balmoral Reef (BR) and Conway Reef (CR) microplates. Sufficient heat flow observations allow Kriging to resolve additional ridge segments and transform faults outlining BR and CR (b). The difference between similarity and Kriging (c) is discordant and difficult to interpret. Bold and thin white lines represent the subduction zone segment boundary and plate depth, respectively, as defined by Syracuse & Abers (2006). Heat flow data and similarity prediction from Lucaleau (2019).

338 **4 Discussion**339 **4.1 Kriging Optimization**

340 Variogram model ranges characterize the maximum separation distance at which
 341 pairs of points are spatially dependent (Matheron, 1963). Therefore, the range is the most
 342 important parameter to evaluate when considering spatial continuity of heat flow.

343 **4.2 The First and Third Laws of Geography**

344 The Third Law of Geography states that *two points with similar geographic con-*
 345 *figurations should have similar values.* In the context of heat flow near subduction sys-
 346 tems and associated spreading centers, the Third Law produces interpolations that high-
 347 light discrete tectonic features (spreading centers and large fault systems) with complex
 348 regional texture. At first glance the textural complexity may be misconstrued as real-
 349 istic interpolations, but is merely an artifact of the similarity method. The texture pre-
 350 dicted by similarity is artificial insofar as it does not represent spatial changes in sur-
 351 face heat flow. Rather each prediction location represents an independent assignment
 352 of heat flow by association to all other locations with similar geographic configurations
 353 (Goutorbe et al., 2011; Lucaleau, 2019; Zhu et al., 2018). The extent to which simila-
 354 rity predictions represent real changes of heat flow in space is entirely dependent on the
 355 reliability of the Third Law, the quality of the physical proxies, and the selected com-
 356 bination of proxies used for interpolation.

357 We note a few inconsistencies with Lucaleau (2019)'s similarity predictions in the
 358 domains considered in this study. First, Lucaleau (2019)'s predictions systematically over-
 359 predict heat flow near spreading centers, justifying an adjustment to their algorithm. Sec-
 360 ond, known tectonic features within the tectonically-complex region near Vanuatu may
 361 be better resolved by Kriging than Lucaleau (2019)'s predictions. It is important to note,
 362 however, that Vanuatu is the only case where Kriging resolves tectonic features that simi-
 363 larity does not; the trend is otherwise opposite. Moreover, the inconsistencies near Van-
 364 uatu do not imply algorithmic issues and can likely be resolved by similarity using a finer-
 365 scale grid.

366 The more important inconsistencies are general discordance between similarity pre-
 367 dictions and observations. Disagreements with observations imply failures of the Third

368 Law, which are not easily correctable algorithmically. Cross-validation statistics given
369 by Lucaleau (2019) demonstrate good agreement with observations in general. The cross-
370 validation error may be sufficiently small for calculating global heat flux and probing other
371 relevant questions on the global scale. However, testing hypotheses which require sam-
372 pling heat flow on the subduction zone segment scale should carefully consider where pre-
373 dictions and observations differ, regardless of the interpolation method (discussed fur-
374 ther below).

375 Unlike the Third Law, the First Law of Geography by definition does not allow dis-
376 cordance between predictions and observations. This fact can be colloquially stated as
377 *everything is related, but nearer things are more related (and points at the exact same*
378 *location are perfectly related)*. More formally, the covariance of two points at the same
379 location must be zero. Comparing the First and Third Laws reveals further asymmetry
380 in the sources of errors. Sources of interpolation error include: 1) quality of heat flow
381 observations (First & Third Law), 2) variance of predictions at unknown locations (First
382 & Third Law), 3) residuals of predictions at known locations (Third Law), 4) Kriging
383 weights (variogram model; First Law), 5) variances of physical proxies (Third Law), 6)
384 combinations of physical proxies (Third Law), 7) similarity weights (similarity model;
385 Third Law). Interpolation uncertainty is easier to conceptualize and quantify for First
386 Law interpolations than Third Law interpolations.

387 Arguments in favor of First or Third Law interpolations, however, are not easily
388 generalized. Third Law interpolations are justified in cases with inadequate heat flow
389 observations (e.g. Scotia and New Britain Solomon). First Law interpolations are arguably
390 more favorable in all cases with adequate heat flow observations because 1) enough ob-
391 servations will resolve important features, 2) spatial dependency is respected, and 3) there
392 are fewer sources of uncertainty. However, it is difficult to know what “adequate” ob-
393 servational density and spatial coverage are *a priori*. In any case, it may not be feasi-
394 ble to achieve adequate observational density and spatial coverage due to time and bud-
395 get constraints. Therefore, hypotheses and sampling strategies should be constructed with
396 careful consideration of whether First or Third Law interpolations are more appropri-
397 ate on a case-by-case basis.

398 **4.3 Heat Flow Sampling and Hypothesis Testing**

399 Testing hypotheses relating to subduction dynamics and seismicity require sam-
400 pling of heat flow. Sampling in previous work commonly uses a three-part strategy: 1)
401 draw a cross-section line perpendicular to the trench, 2) draw a rectangle with arbitrary
402 width bisected by the section line, 3) gather all heat flow observations within the rect-
403 angle and project them onto the section line. This sampling strategy is simple and most
404 effective for section lines with nearby, equally spaced, high-density observations (almost
405 never the case). The method increasingly violates the First Law as the size of the sam-
406 pling rectangle increases, including more disparate points. This strategy must also be
407 repeated many times along strike to fully characterize the spatial distribution of heat flow
408 near subduction zone segments. Repeated sampling along strike has not been done in
409 previous studies.

410 The Third Law has been used successfully in calculating global surface heat flux
411 [] and testing lithospheric cooling models [].

412 **5 Conclusions**413 **Acknowledgments**414 **Appendix**415 **Heat flow observations and predictions**

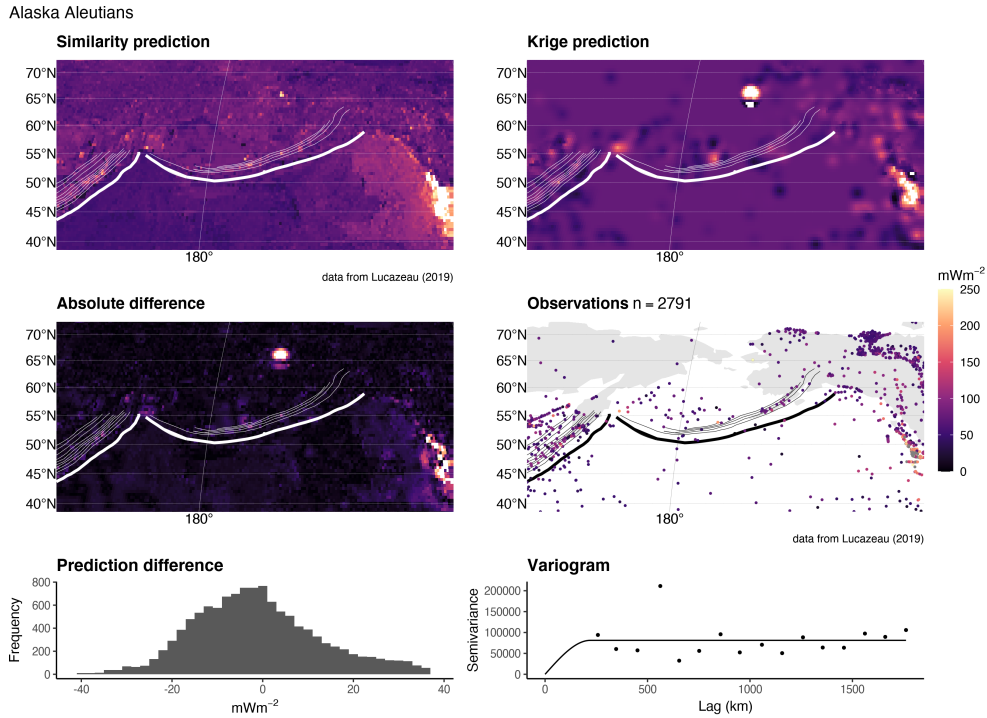


Figure 11: Similarity vs. Kriging predictions for Alaska Aleutians.

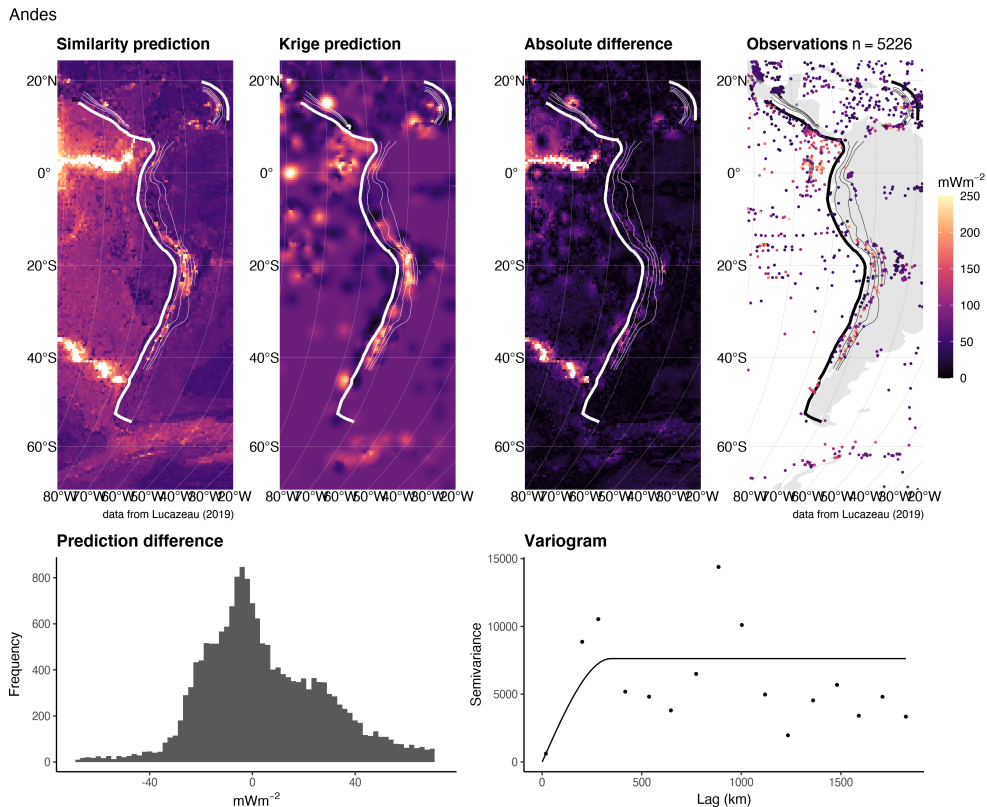


Figure 12: Similarity vs. Kriging predictions for the Andes.

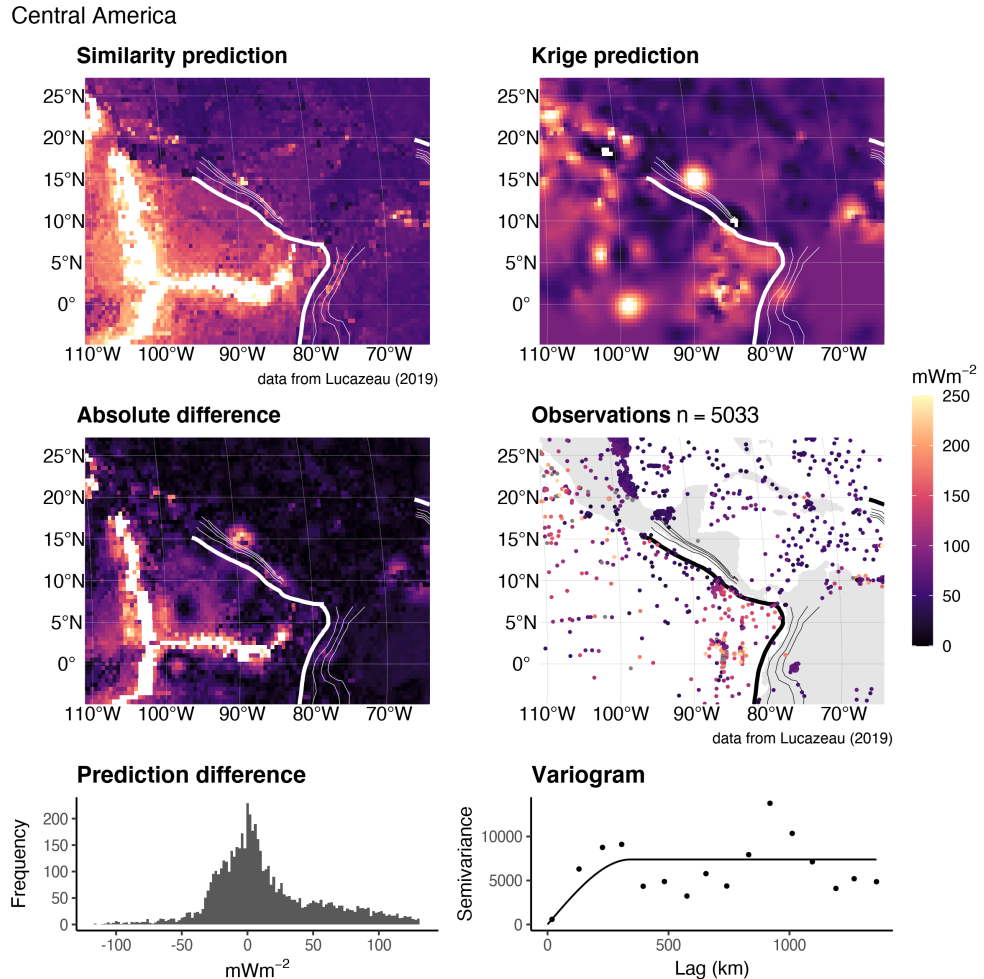


Figure 13: Similarity vs. Kriging predictions for Central America.

Kamchatka Marianas

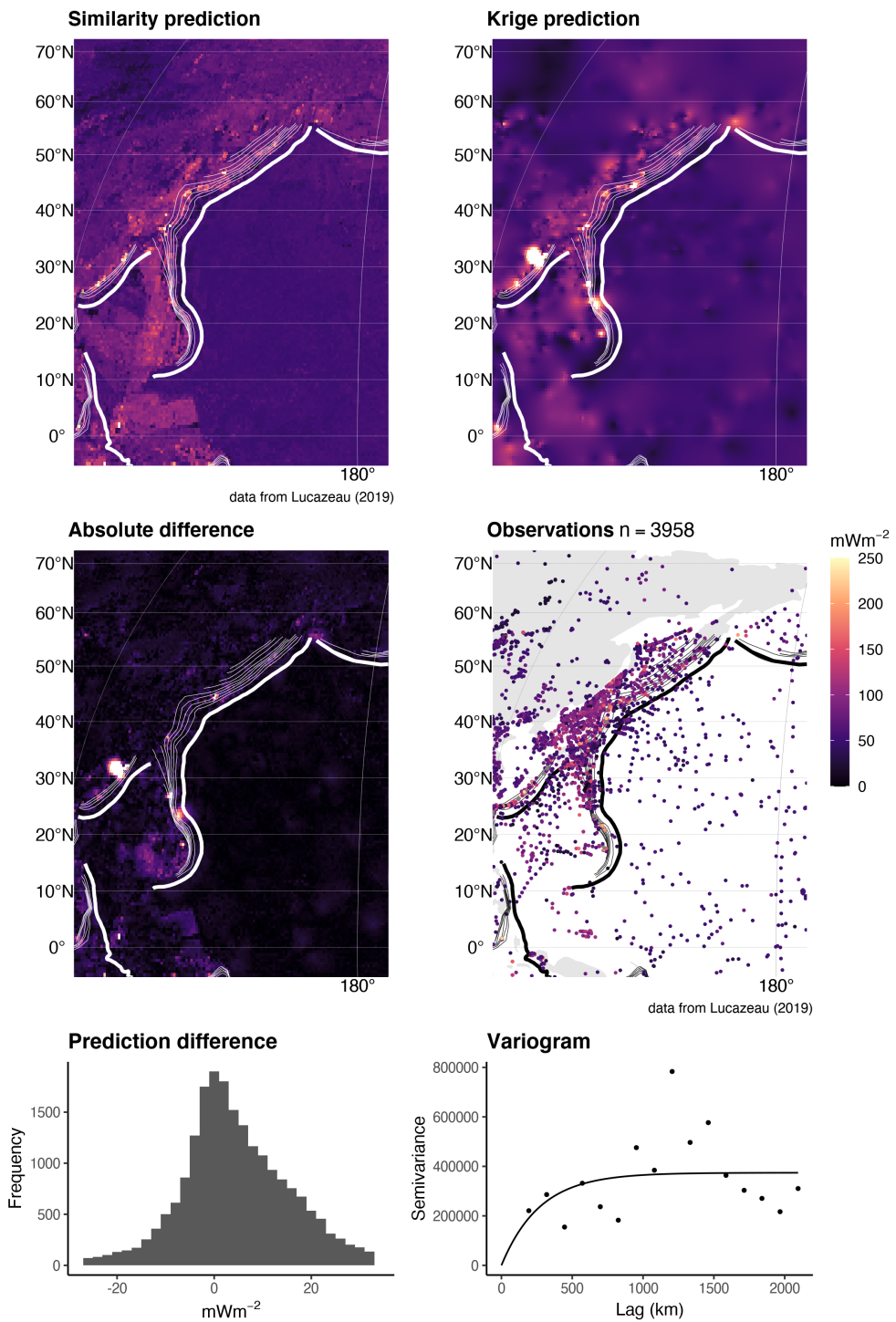


Figure 14: Similarity vs. Kriging predictions for Kamchatka Marianas.

Kyushu Ryukyu

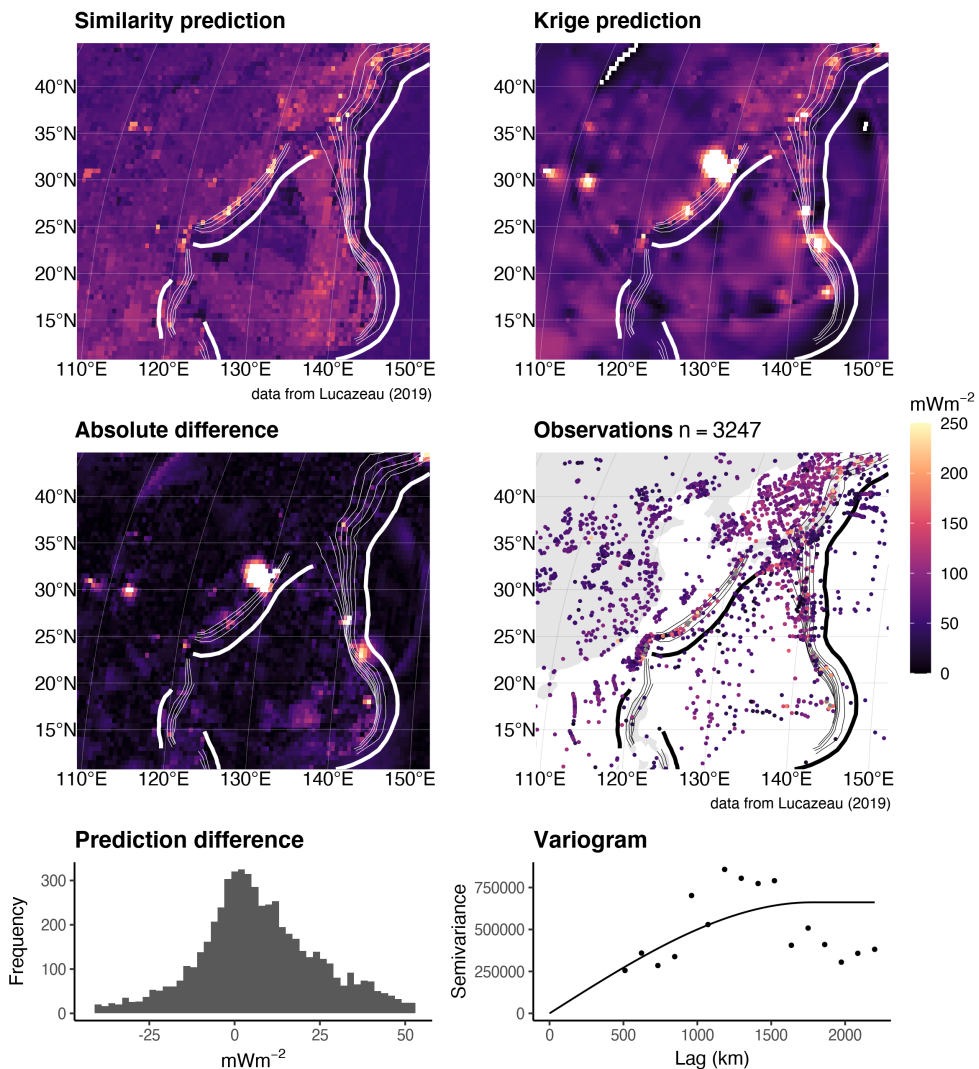


Figure 15: Similarity vs. Kriging predictions for Kyushu Ryukyu.

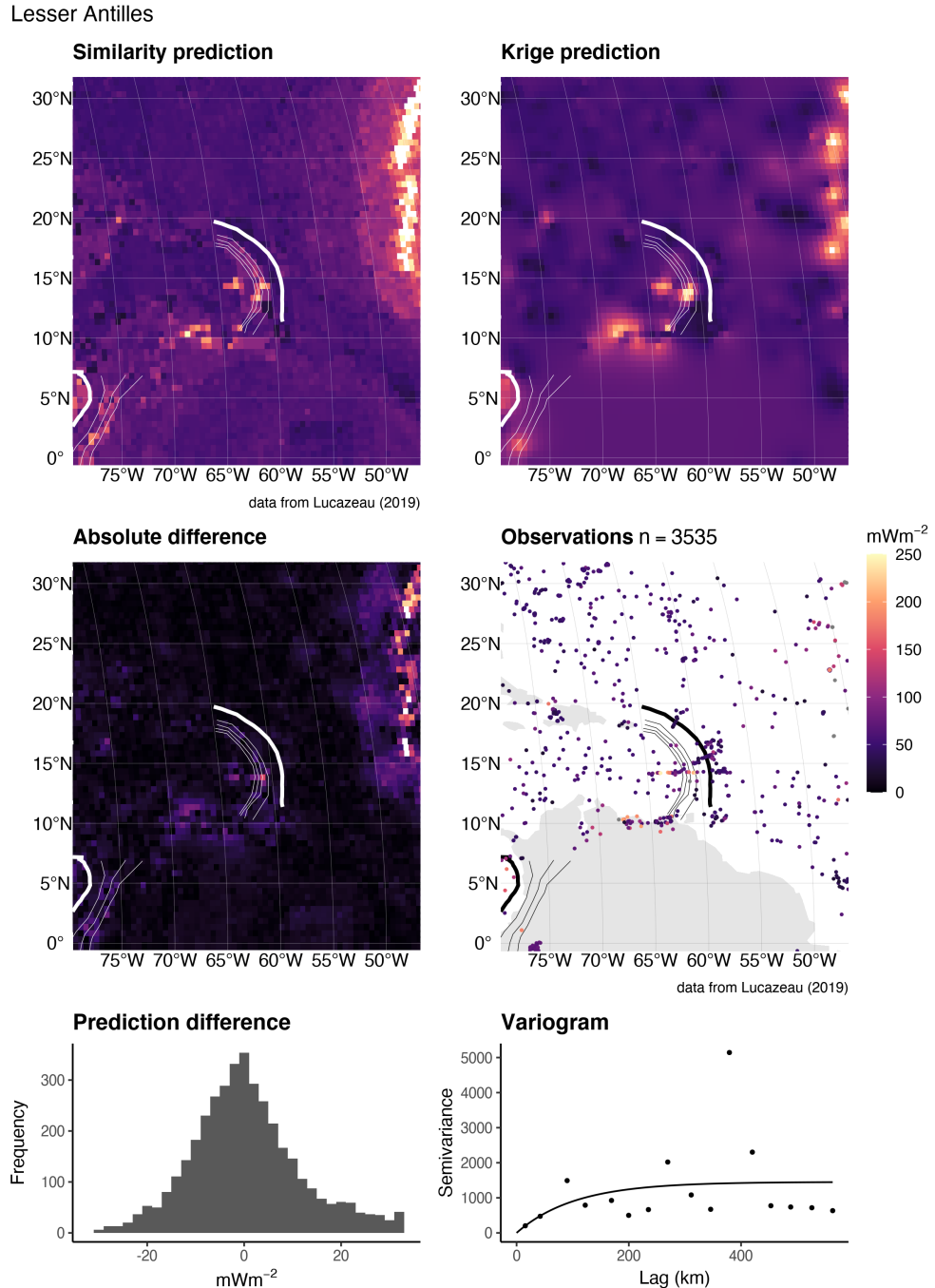


Figure 16: Similarity vs. Kriging predictions for the Lesser Antilles.

N. Philippines

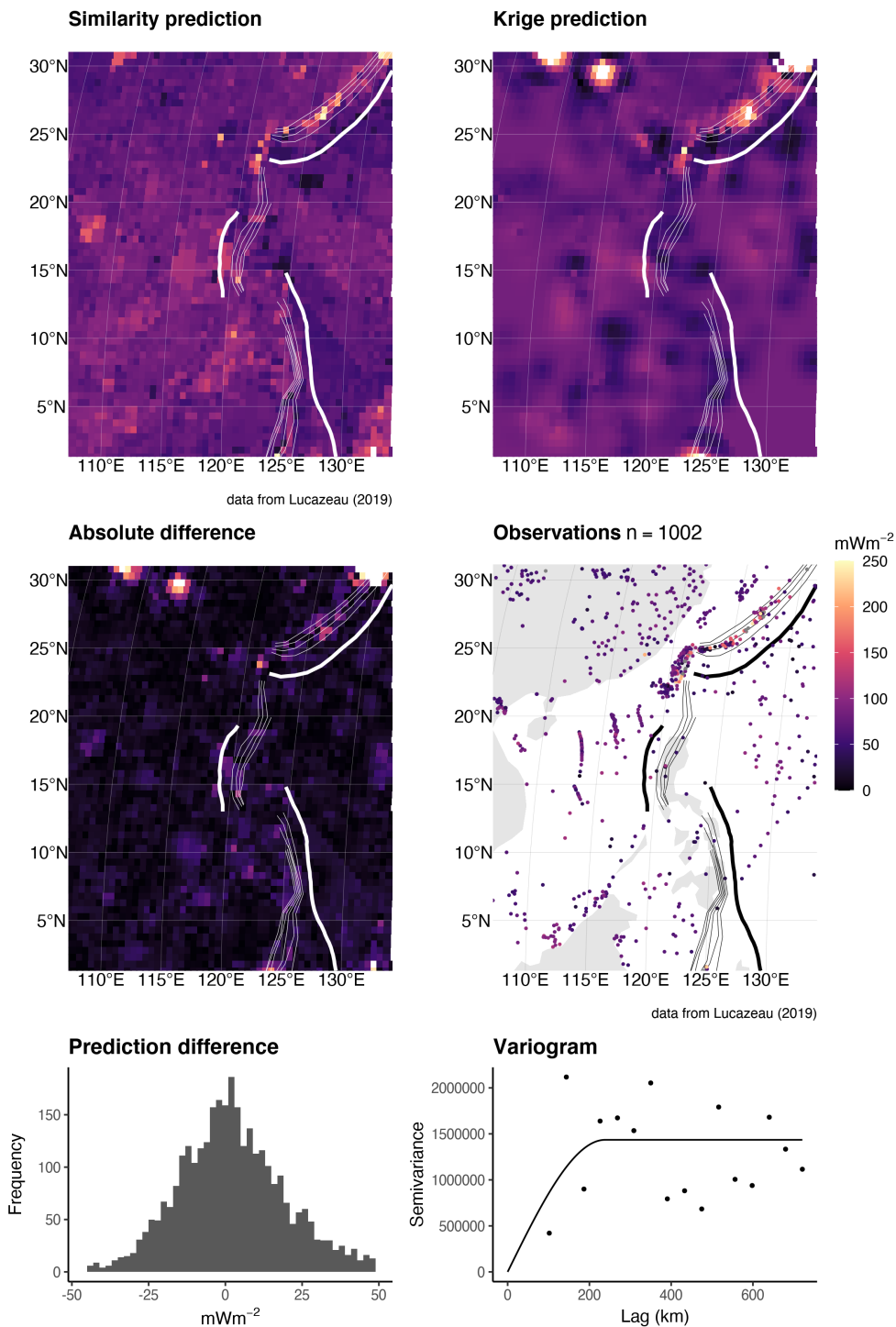


Figure 17: Similarity vs. Kriging predictions for N. Philippines.

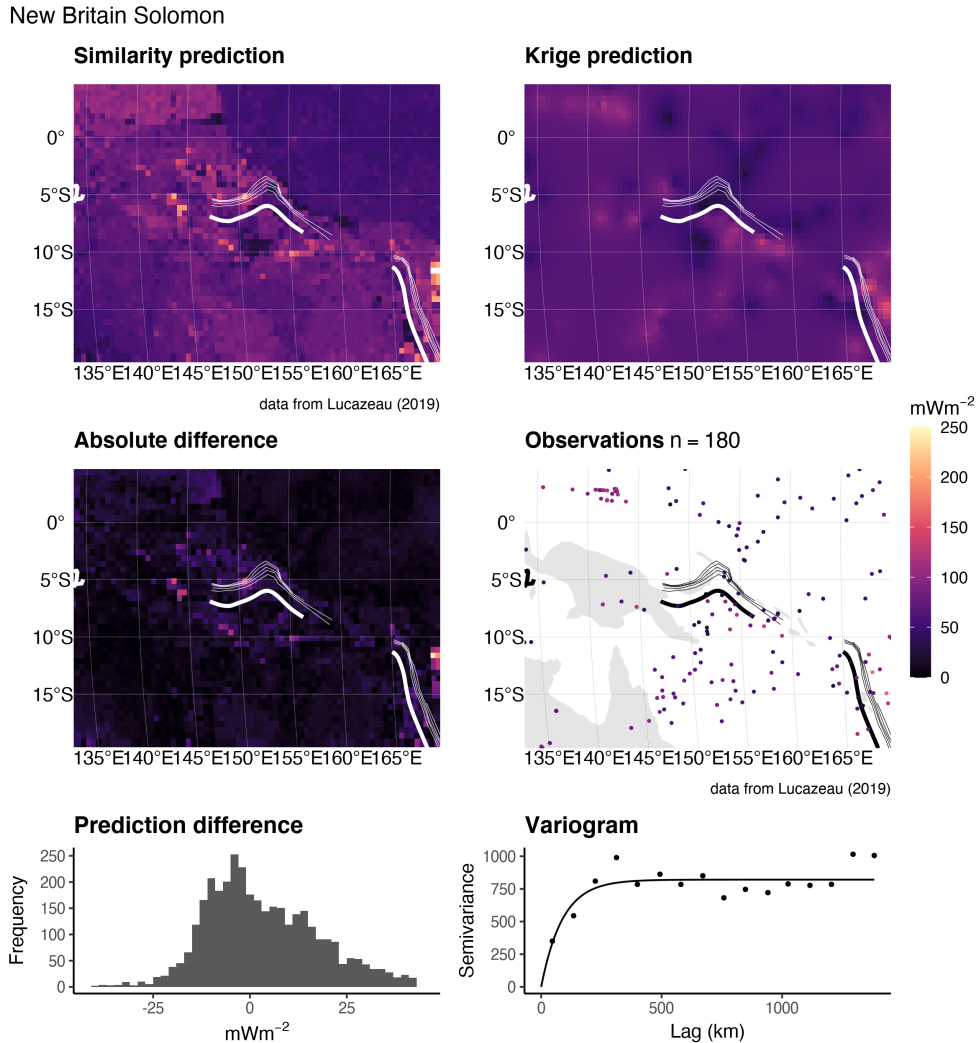


Figure 18: Similarity vs. Kriging predictions for New Britain Solomon.

S. Philippines

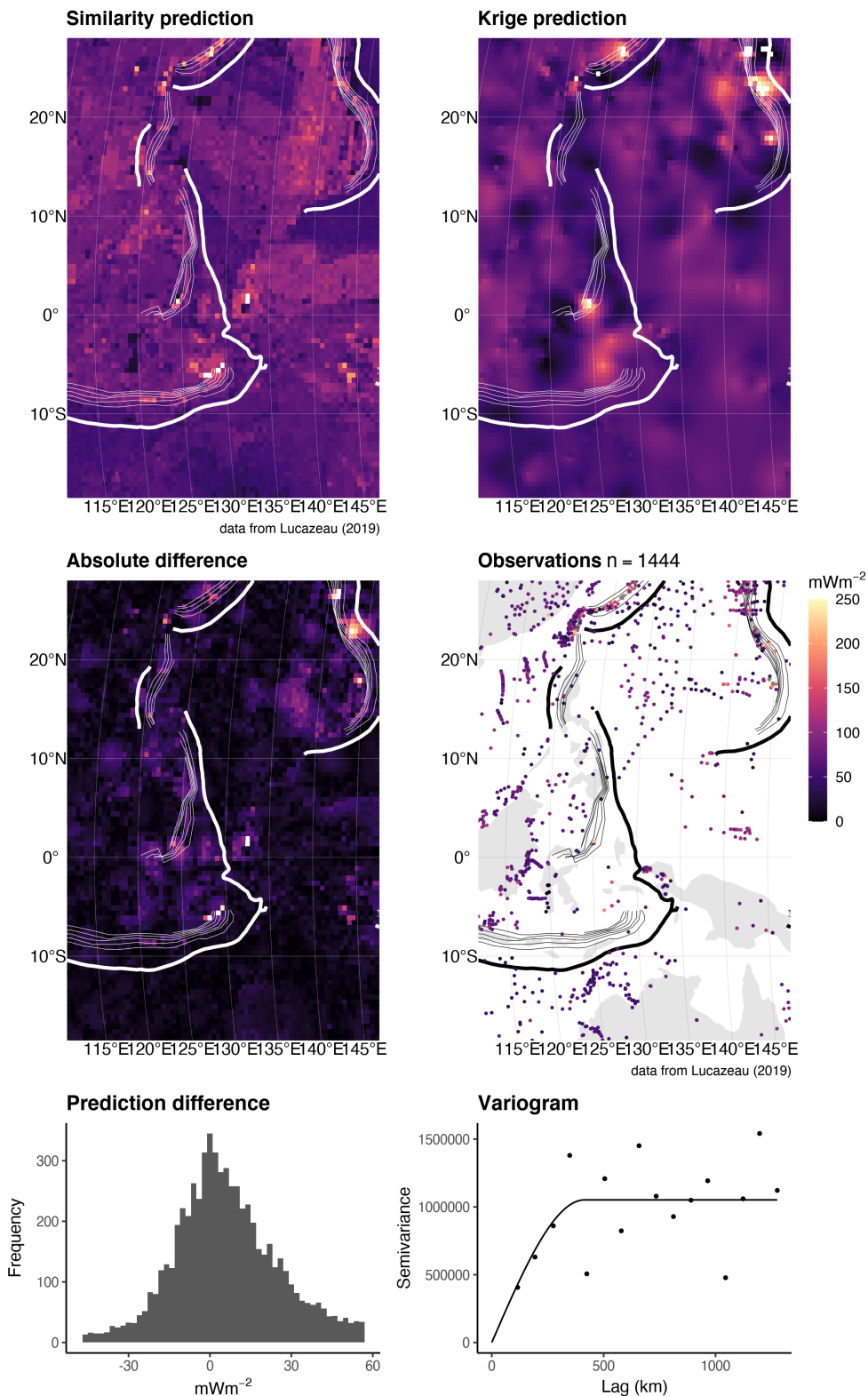


Figure 19: Similarity vs. Kriging predictions for S. Philippines.

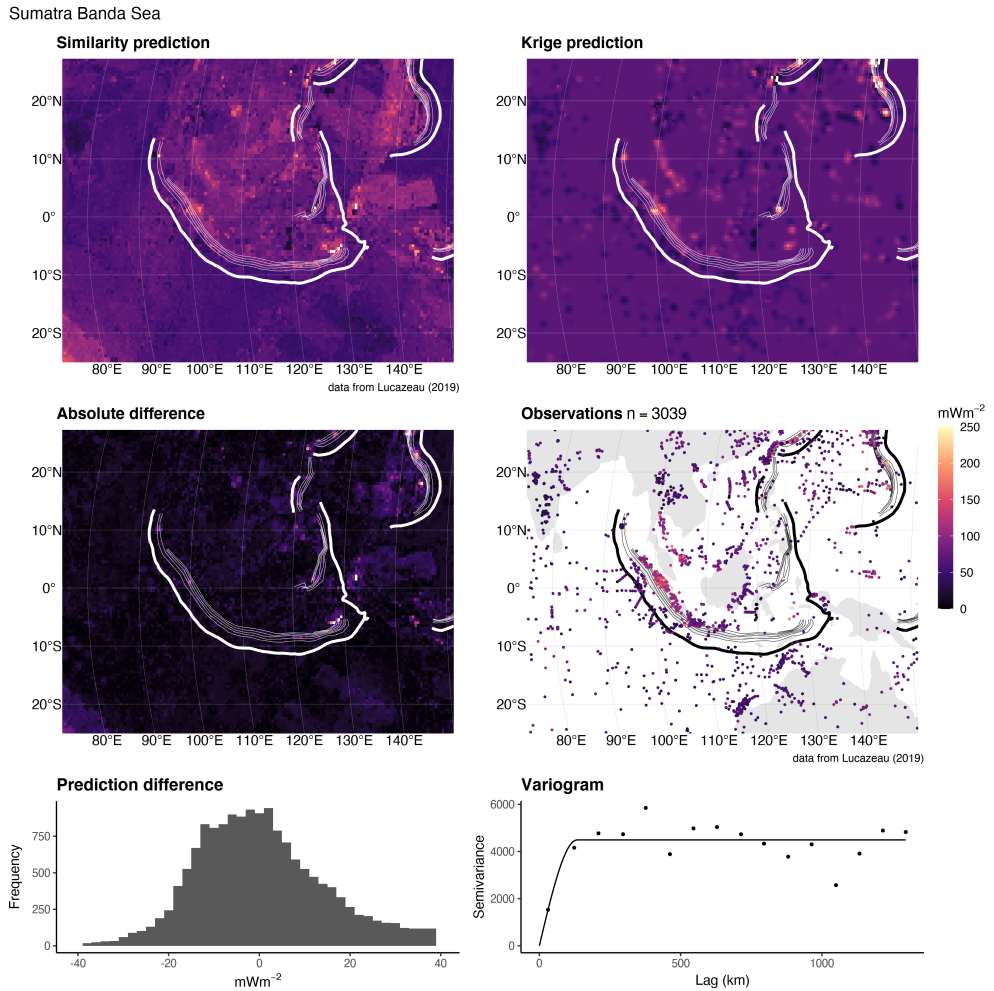


Figure 20: Similarity vs. Kriging predictions for Sumatra Banda Sea.

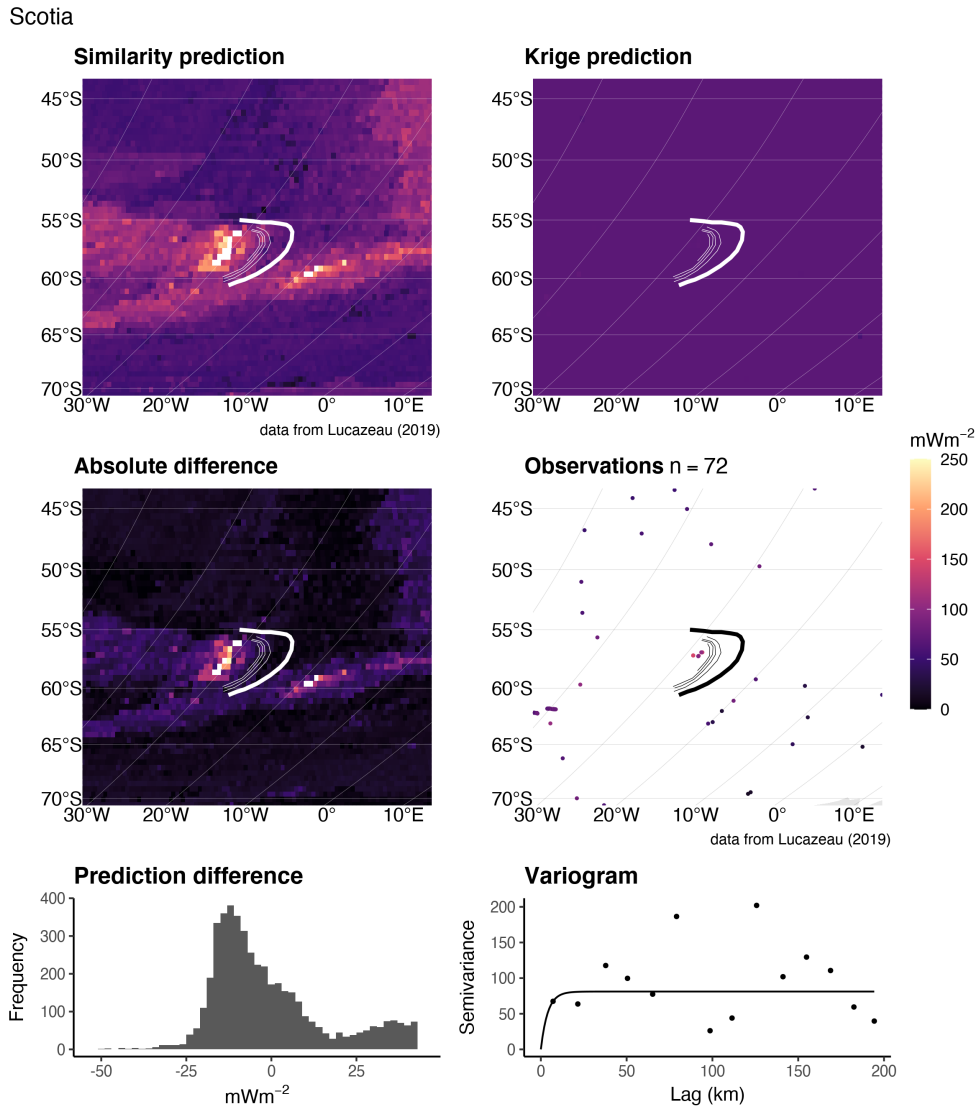


Figure 21: Similarity vs. Kriging predictions for Scotia.

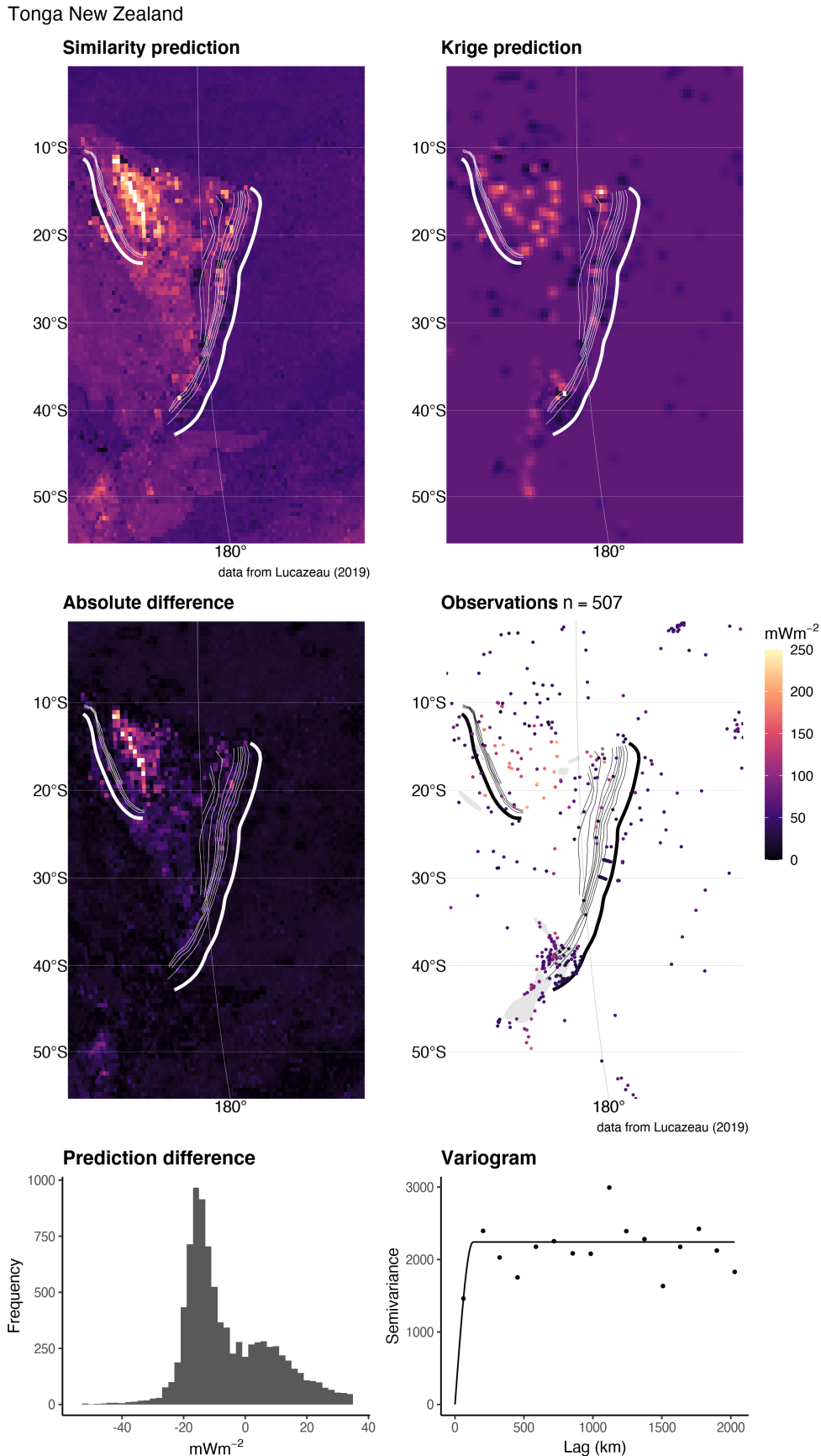


Figure 22: Similarity vs. Kriging predictions for Tonga New Zealand.

Vanuatu

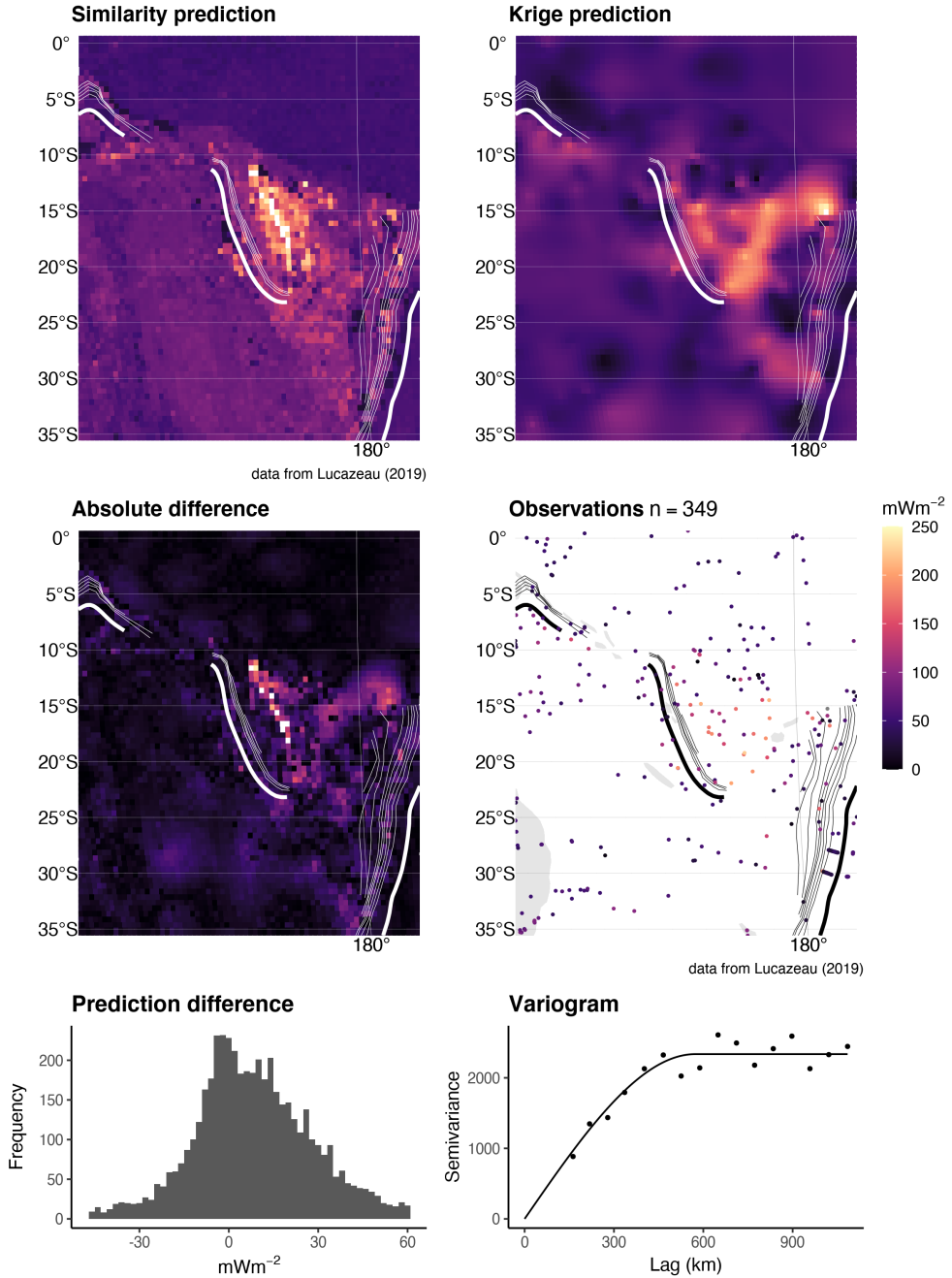


Figure 23: Similarity vs. Kriging predictions for Vanuatu.

416 **References**

- 417 Bárdossy, A. (1997). Introduction to geostatistics. *Institute of Hydraulic Engineering,*
 418 *University of Stuttgart.*
- 419 Chapman, D. S., & Pollack, H. N. (1975). Global heat flow: A new look. *Earth and Plan-*
 420 *etary Science Letters, 28*(1), 23–32.
- 421 Chiles, J.-P., & Delfiner, P. (2009). *Geostatistics: Modeling spatial uncertainty* (Vol. 497).
 422 John Wiley & Sons.
- 423 Cressie, N. (2015). *Statistics for spatial data*. John Wiley & Sons.
- 424 Currie, C., & Hyndman, R. D. (2006). The thermal structure of subduction zone back
 425 arcs. *Journal of Geophysical Research: Solid Earth, 111*(B8).
- 426 Currie, C., Wang, K., Hyndman, R. D., & He, J. (2004). The thermal effects of steady-
 427 state slab-driven mantle flow above a subducting plate: The Cascadia subduction zone
 428 and backarc. *Earth and Planetary Science Letters, 223*(1-2), 35–48.
- 429 Davies, J. H. (2013). Global map of solid earth surface heat flow. *Geochemistry, Geo-*
 430 *physics, Geosystems, 14*(10), 4608–4622.
- 431 Fourier, J. (1827). Mémoire sur les températures du globe terrestre et des espaces planétaires.
 432 *Mémoires de l'Académie Royale Des Sciences de l'Institut de France, 7*, 570–604.
- 433 Furlong, K. P., & Chapman, D. S. (2013). Heat flow, heat generation, and the thermal
 434 state of the lithosphere. *Annual Review of Earth and Planetary Sciences, 41*, 385–
 435 410.
- 436 Furukawa, Y. (1993). Depth of the decoupling plate interface and thermal structure un-
 437 der arcs. *Journal of Geophysical Research: Solid Earth, 98*(B11), 20005–20013.
- 438 Gao, X., & Wang, K. (2014). Strength of stick-slip and creeping subduction megathrusts
 439 from heat flow observations. *Science, 345*(6200), 1038–1041.
- 440 Goldberg, D. E. (1989). Genetic algorithms in search. *Optimization, and MachineLearn-*
 441 *ing.*

- 442 Goodchild, M. F. (2004). The validity and usefulness of laws in geographic information
443 science and geography. *Annals of the Association of American Geographers*, 94(2),
444 300–303.
- 445 Goovaerts, P. (1997). *Geostatistics for natural resources evaluation*. Oxford University
446 Press on Demand.
- 447 Goutorbe, B., Poort, J., Lucaleau, F., & Raillard, S. (2011). Global heat flow trends re-
448 solved from multiple geological and geophysical proxies. *Geophysical Journal Inter-
449 national*, 187(3), 1405–1419.
- 450 Gräler, B., Pebesma, E., & Heuvelink, G. (2016). Spatio-temporal interpolation using
451 gstat. *The R Journal*, 8, 204–218. Retrieved from <https://journal.r-project.org/archive/2016/RJ-2016-014/index.html>
- 452
- 453 Hasterok, D. (2013). A heat flow based cooling model for tectonic plates. *Earth and Plan-
454 etary Science Letters*, 361, 34–43.
- 455 Hasterok, D., & Chapman, D. (2008). Global heat flow: A new database and a new ap-
456 proach. In *AGU fall meeting abstracts* (Vol. 2008, pp. T21C–1985).
- 457 Hasterok, D., Chapman, D., & Davis, E. (2011). Oceanic heat flow: Implications for global
458 heat loss. *Earth and Planetary Science Letters*, 311(3-4), 386–395.
- 459 Jennings, S., & Hasterok, D. (2021). HeatFlow.org. *Heatflow.org*. Retrieved from <http://heatflow.org/>
- 460
- 461 Kerswell, B. C., Kohn, M. J., & Gerya, T. V. (2020). Backarc lithospheric thickness and
462 serpentine stability control slab-mantle coupling depths in subduction zones. *Earth
463 and Space Science Open Archive*, 34. [https://doi.org/10.1002/essoar.10503710
464 .1](https://doi.org/10.1002/essoar.10503710.1)
- 465 Krige, D. G. (1951). A statistical approach to some basic mine valuation problems on
466 the witwatersrand. *Journal of the Southern African Institute of Mining and Metal-
467 lurgy*, 52(6), 119–139.
- 468 Lee, W. H., & Uyeda, S. (1965). Review of heat flow data. *Terrestrial Heat Flow*, 8, 87–
469 190.

- 470 Li, Z., Zhang, X., Clarke, K. C., Liu, G., & Zhu, R. (2018). An automatic variogram mod-
 471 eling method with high reliability fitness and estimates. *Computers & Geosciences*,
 472 120, 48–59.
- 473 Lucazeau, F. (2019). Analysis and mapping of an updated terrestrial heat flow data set.
 474 *Geochemistry, Geophysics, Geosystems*, 20(8), 4001–4024.
- 475 Matheron, G. (1963). Principles of geostatistics. *Economic Geology*, 58(8), 1246–1266.
- 476 Matheron, G. (2019). *Matheron's theory of regionalized variables*. International Asso-
 477 ciation for.
- 478 Parsons, B., & Sclater, J. G. (1977). An analysis of the variation of ocean floor bathymetry
 479 and heat flow with age. *Journal of Geophysical Research*, 82(5), 803–827.
- 480 Pebesma, E. (2004). Multivariable geostatistics in S: The gstat package. *Computers &*
 481 *Geosciences*, 30, 683–691.
- 482 Pebesma, E. (2018). Simple Features for R: Standardized Support for Spatial Vector Data.
 483 *The R Journal*, 10(1), 439–446. <https://doi.org/10.32614/RJ-2018-009>
- 484 Pollack, H. N., & Chapman, D. S. (1977). On the regional variation of heat flow, geotherms,
 485 and lithospheric thickness. *Tectonophysics*, 38(3-4), 279–296.
- 486 Pollack, H. N., Hurter, S. J., & Johnson, J. R. (1993). Heat flow from the earth's inte-
 487 rior: Analysis of the global data set. *Reviews of Geophysics*, 31(3), 267–280.
- 488 PROJ contributors. (2021). *PROJ coordinate transformation software library*. Open Source
 489 Geospatial Foundation. Retrieved from <https://proj.org/>
- 490 Rudnick, R. L., McDonough, W. F., & O'Connell, R. J. (1998). Thermal structure, thick-
 491 ness and composition of continental lithosphere. *Chemical Geology*, 145(3-4), 395–
 492 411.
- 493 Sclater, J. G., & Francheteau, J. (1970). The implications of terrestrial heat flow obser-
 494 vations on current tectonic and geochemical models of the crust and upper mantle
 495 of the earth. *Geophysical Journal International*, 20(5), 509–542.
- 496 Scrucca, L. (2013). GA: A package for genetic algorithms in r. *Journal of Statistical Soft-
 497 ware*, 53(4), 1–37.

- 498 Scrucca, L. (2016). On some extensions to GA package: Hybrid optimisation, parallelisation and islands evolution. *arXiv Preprint arXiv:1605.01931*.
- 500 Shapiro, N. M., & Ritzwoller, M. H. (2004). Inferring surface heat flux distributions guided
501 by a global seismic model: Particular application to antarctica. *Earth and Planetary
502 Science Letters*, 223(1-2), 213–224.
- 503 Stein, C. A., & Stein, S. (1992). A model for the global variation in oceanic depth and
504 heat flow with lithospheric age. *Nature*, 359(6391), 123–129.
- 505 Stein, C. A., & Stein, S. (1994). Constraints on hydrothermal heat flux through the oceanic
506 lithosphere from global heat flow. *Journal of Geophysical Research: Solid Earth*, 99(B2),
507 3081–3095.
- 508 Syracuse, E. M., & Abers, G. A. (2006). Global compilation of variations in slab depth
509 beneath arc volcanoes and implications. *Geochemistry, Geophysics, Geosystems*, 7(5).
- 510 Wada, I., & Wang, K. (2009). Common depth of slab-mantle decoupling: Reconciling
511 diversity and uniformity of subduction zones. *Geochemistry, Geophysics, Geosystems*,
512 10(10).
- 513 Wilkinson, M. D., Dumontier, M., Aalbersberg, Ij. J., Appleton, G., Axton, M., Baak,
514 A., et al. (2016). The FAIR guiding principles for scientific data management and
515 stewardship. *Scientific Data*, 3(1), 1–9.
- 516 Zhu, A.-X., Lu, G., Liu, J., Qin, C.-Z., & Zhou, C. (2018). Spatial prediction based on
517 third law of geography. *Annals of GIS*, 24(4), 225–240.